

## The Implications of Local Fluctuations in the Galactic Midplane for Dynamical Analysis in the Gaia Era

Angus Beane<sup>1,2</sup>, Robyn E. Sanderson<sup>2,1</sup>, Melissa K. Ness<sup>3,1</sup>, Kathryn V. Johnston<sup>3,1</sup>, Douglas Grion Filho<sup>3</sup>, Mordecai-Mark Mac Low<sup>4,1</sup>, Daniel Anglés-Alcázar<sup>1</sup>, David W. Hogg<sup>5,6,1,7</sup>, and Chervin F. P. Laporte<sup>8,9</sup> Center for Computational Astrophysics, Flatiron Institute, 162 5th Ave., New York, NY 10010, USA; abeane@sas.upenn.edu Department of Physics & Astronomy, University of Pennsylvania, 209 South 33rd St., Philadelphia, PA 19104, USA Department of Astronomy, Columbia University, 550 West 120th St., New York, NY 10027, USA <sup>4</sup> Department of Astrophysics, American Museum of Natural History, Central Park West at 79th St., New York, NY 10024, USA <sup>5</sup> Center for Cosmology and Particle Physics, Department of Physics, New York University, 726 Broadway, New York, NY 10003, USA

<sup>6</sup> Center for Data Science, New York University, 60 5th Ave., New York, NY 10011, USA Max-Planck-Institut für Astronomie, Königstuhl 17, D-69117 Heidelberg, Germany <sup>8</sup> Department of Physics & Astronomy, University of Victoria, 3800 Finnerty Rd., Victoria, BC, V8P 4HN, Canada Received 2019 May 21; revised 2019 August 8; accepted 2019 August 19; published 2019 September 25

#### Abstract

Orbital properties of stars, computed from their six-dimensional phase-space measurements and an assumed Galactic potential, are used to understand the structure and evolution of the Galaxy. Stellar actions, computed from orbits, have the attractive quality of being invariant under certain assumptions and are therefore used as quantitative labels of a star's orbit. We report a subtle but important systematic error that is induced in the actions as a consequence of local midplane variations expected for the Milky Way. This error is difficult to model because it is non-Gaussian and bimodal, with neither mode peaking on the null value. An offset in the vertical position of the Galactic midplane of  $\sim$ 15 pc for a thin disk-like orbit or  $\sim$ 120 pc for a thick disk-like orbit induces a 25% systematic error in the vertical action J<sub>z</sub>. In Feedback in Realistic Environments simulations of Milky Way-mass galaxies, these variations are on the order of  $\sim$ 100 pc at the solar circle. From observations of the mean vertical velocity variation of  $\sim 5-10 \,\mathrm{km \, s^{-1}}$  with radius, we estimate that the Milky Way midplane variations are  $\sim$ 60–170 pc, consistent with three-dimensional dust maps. Action calculations and orbit integrations, which assume the global and local midplanes are identical, are likely to include this induced error, depending on the volume considered. Variation in the local standard of rest or distance to the Galactic center causes similar issues. The variation of the midplane must be taken into account when performing dynamical analysis across the large regions of the disk accessible to Gaia and future missions.

Unified Astronomy Thesaurus concepts: Milky Way disk (1050); Milky Way dynamics (1051); Milky Way evolution (1052); Galaxy structure (622); Orbits (1184); Stellar dynamics (1596)

#### 1. Introduction

Our understanding of the Milky Way is currently undergoing a revolution as a result of Gaia Data Release 2 (DR2). Recent major discoveries include the affirmation of remnants of a major merger (Belokurov et al. 2018; Helmi et al. 2018; Koppelman et al. 2018; Lancaster et al. 2019; Mackereth et al. 2019) hinted at in pre-Gaia work (e.g., Meza et al. 2005; Navarro et al. 2011), a phase-space "spiral" in the solar neighborhood (Antoja et al. 2018) possibly indicating local substructure infall (Binney & Schönrich 2018; Laporte et al. 2019b), and a gap suggestive of perturbation by a dark matter substructure in the tidal stream GD1 (Bonaca et al. 2019; Price-Whelan & Bonaca 2018). These discoveries all indicate that the Milky Way's stellar distribution, which demonstrably departs significantly from axisymmetry, is undergoing phase mixing and dynamical interactions across a range of spatial and temporal scales.

The assumption of a global, axisymmetric Galactocentric coordinate system (Binney & Tremaine 2008) underlies much of the quantitative analysis of the mechanisms that give rise to these signatures. In order to construct such a system, the Sun's relative position and velocity must be defined and measured both precisely and accurately. This involves determining the angular position of and distance to the Galactic center, the orientation of and distance to the Galactic midplane, and the local standard of rest (LSR). We review and discuss the observational efforts to measure these parameters in Section 4.2.

Once a Galactocentric coordinate system has been established and a six-dimensional (6D) phase-space measurement of a star has been made, it is often desirable to convert this measurement into action space to concisely summarize its projected orbit, model the stellar distribution function, or find stars with similar dynamical properties. Actions are conserved quantities that describe the orbit of a star under the assumption of regular, bound orbits in a system where the equations of motion are separable in a particular coordinate system. They are the cyclical integral of the canonical momentum over its conjugate position

$$J_i \equiv \frac{1}{2\pi} \oint_{\text{orbit}} p_i \, dx_i, \tag{1}$$

where  $p_i$  are the conjugate momenta. Under the assumption of axisymmetry, i = R,  $\phi$ , z are the radial, azimuthal, and vertical coordinates, respectively, in a cylindrical coordinate system. In a slowly evolving axisymmetric potential, these actions are invariant and  $J_{\phi} \equiv L_z$ , where  $L_z$  is the z-component of the

<sup>&</sup>lt;sup>9</sup> CITA National Fellow.

angular momentum (Binney & Tremaine 2008; Sellwood 2014).

With the advent of 6D phase-space measurements over a relatively large ( $\gtrsim 2$  kpc) volume from the *Gaia* satellite, the study of stellar actions has gained new popularity. One reason is dimensionality reduction—an individual stellar orbit is concisely described by three actions, as opposed to six phase-space coordinates. Second, under the assumption of a phase-mixed system, the dynamical properties of a population of stars should be uniquely a function of their actions and independent of the conjugate angles. This allows one to use actions to study the relationship between orbital properties of stars and other intrinsic, and, at least partially, invariant properties such as age or metallicity (Beane et al. 2018; Sanders & Das 2018; Ting & Rix 2018; Bland-Hawthorn et al. 2019; Das et al. 2019; Gandhi & Ness 2019). Actions also provide a convenient basis for constructing models of the stellar distribution function (e.g., Jeans 1915; Villumsen & Binney 1985; Trick et al. 2017), or for associating stars with similar dynamical properties, e.g., to potentially determine membership in moving groups.

If the system being considered departs from axisymmetry in a significant and/or non-adiabatic way, the actions computed using an axisymmetric approximation to the true potential can exhibit cyclic dependence on the orbital phase (or time at which the star's position and velocity are observed), large-scale migration, or diffusion from their initial values. In the Milky Way, stellar actions are expected to diffuse on short timescales due to scattering with gas clouds and to evolve on longer timescales in the case of orbits near resonances with spiral arms, bar(s), and other large-scale perturbations (Sellwood 2014). For this reason, actions have been used to study stellar scattering in the Milky Way disk using the improved astrometry of Gaia DR2 and various age catalogs (Beane et al. 2018; Ting & Rix 2018). Actions have also been used to study different models of spiral structure in the Milky Way (Sellwood et al. 2019). Characteristics of the distribution of stars in the extended solar neighborhood in action space are discussed in Trick et al. (2019).

The true Galactic potential is not strictly axisymmetric, beyond even the typically quoted gas clouds, spiral arms, and bar(s). The presence of disk oscillations has been known since its observation in H I by Kerr (1957). The presence of a northsouth asymmetry in stellar number density and velocity in the solar neighborhood has been found in Sloan Digital Sky Survey (SDSS) data (Widrow et al. 2012), and in velocity in the Large Sky Area Multi-Object Fiber Spectroscopic Telescope (LAMOST) survey (Carlin et al. 2013; Xu et al. 2015), and RAdial Velocity Experiment (RAVE) data (Williams et al. 2013). Beyond the solar neighborhood, low-latitude overdensities have been observed, e.g., the Monoceros Ring (Newberg et al. 2002; Crane et al. 2003; Ibata et al. 2003; Slater et al. 2014; Morganson et al. 2016), an overdensity in the direction of the Triangulum and Andromeda galaxies (Martin et al. 2007; Sheffield et al. 2014; Price-Whelan et al. 2015; Xu et al. 2015) and A13 (Sharma et al. 2010; Li et al. 2017), and in the direction of the Galactic Center (Feast et al. 2014). There is evidence that these stellar populations originated from the disk (Price-Whelan et al. 2015; Bergemann et al. 2018; Sheffield et al. 2018). See, e.g., Laporte et al. (2018) for a discussion of these observations.

With the vast improvement in the quality of phase-space measurements due to *Gaia* the assumption of axisymmetry is increasingly inadequate (e.g., Antoja et al. 2018; Laporte et al. 2019b). The presence of the phase-space spiral itself is evidence of disk oscillations (Antoja et al. 2018), but the fact that its strength changes across the disk is further evidence (Bland-Hawthorn et al. 2019; Laporte et al. 2019b). Even if the axisymmetric assumption were close enough for many purposes, the parameters used in axisymmetric models of the Galactic potential may be biased by the non-axisymmetries in the disk.

Such variations in the density of gas and stars cause the local midplane position to vary as a function of radius and azimuth. Stars far from the Sun have a local midplane that differs from our local midplane extrapolated onto their position. Converting positions and velocities of more distant stars from a heliocentric to a Galactocentric coordinate system thus introduces a systematic bias in the z-coordinate. We show that this bias induces non-Gaussian errors in the actions computed for these stars. The further from the solar neighborhood the target star is, the more likely the mismatch will result in large systematic uncertainty, especially in the vertical action  $J_z$ . A similar argument applies to any remaining uncertainty in measurements of the Galactocentric radius of the Sun, and to variations in the LSR.

In Section 2, we describe the general impact coordinate system errors have on the measured actions. In Section 3, we examine the azimuthal variations of the midplane itself in examples from two classes of simulations: cosmological, hydrodynamical, zoom-in simulations of isolated Milky Waymass galaxies from the Feedback in Realistic Environments (FIRE) collaboration<sup>10</sup> (Hopkins et al. 2014; Wetzel et al. 2016; Hopkins et al. 2018), and a controlled N-body simulation of a Sagittarius encounter with a galaxy otherwise tailored to the stellar mass, scale length, and scale height of the Milky Way (Laporte et al. 2018). In Section 4, we discuss the implications of midplane variations, and the resulting systematic uncertainty in the vertical action, for action-space analyses. We also estimate the expected midplane variations of the Milky Way based on the observed velocity variations and threedimensional dust maps. We summarize our main results and conclude in Section 5.

#### 2. Motivation

We first demonstrate the significance to action computations of a systematic offset in the determination of the Galactic midplane, distance to the Galactic center, or LSR. We will find that such offsets are especially important for disk-like orbits. The consequences we explore here may also arise from various other systematic errors. For instance, the axisymmetric Galactic potential model used in many works to compute actions may not be a good description of the true potential—or the parameters used may yield a potential that is systematically incorrect outside an original fitted region. In this work, we assume that the Galaxy is perfectly described by our model axisymmetric potential, and simply explore the consequences of offsets in the Galactocentric coordinate system.

https://fire.northwestern.edu

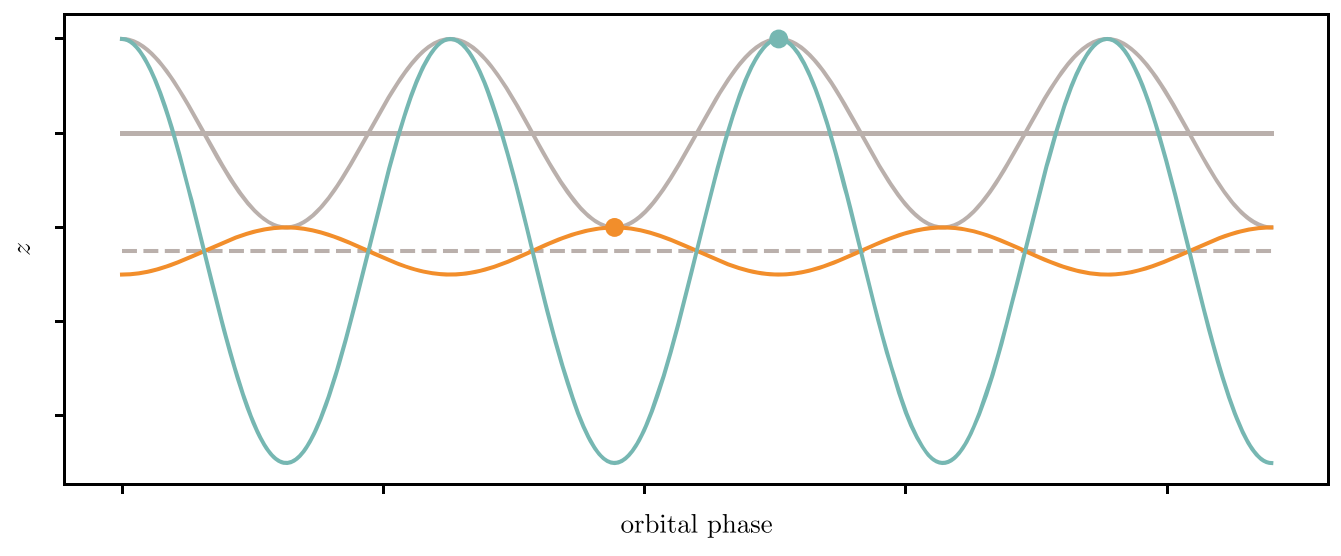


**Figure 1.** Illustration showing the effect an error in the determination of the coordinate midplane can have on orbit integration and action estimation. The *x*-axis shows the orbital phase and the *y*-axis the vertical height. The top gray curve depicts an example "true" orbit oscillating about the true midplane (horizontal solid gray line). Consider an observer who erroneously assumes the midplane is located at the horizontal dashed line. Suppose this observer measures the phase-space position of the star at two different orbital phases (teal and orange points). If the observer were to then integrate the star's orbit using a model potential with the erroneous midplane, they would obtain the teal and orange curves for the star's orbit, respectively. The actions estimated from these two erroneous measurements would subsequently differ, both from each other and from the true measurement (in the potential with the correct coordinate system). Hence an incorrect midplane in the potential model assumed will induce phase dependence in the actions estimated for a given star in that potential.

## 2.1. Effect of Midplane Offset

We present an illustration of an orbit in Figure 1 to show how an inaccurate or erroneous determination of the midplane leads to a dependence on orbital phase of the value of the actions calculated from a point in phase space and an assumed potential model. The *x*-axis corresponds to orbital phase and the *y*-axis to vertical height. The solid gray curve indicates the true orbit of the star as it oscillates around the true midplane. The dashed gray line, offset from the true midplane, is the midplane location used by an observer to integrate the orbit of the star and estimate its actions. The model potential is otherwise identical to the one in which the star is actually moving.

Now suppose this observer makes a measurement of the star's position and velocity at the teal point or the orange point (i.e., at two different orbital phases). Then, the teal and orange curves correspond to the orbits that the observer would compute for each point based on the potential model with the offset midplane. In action space, this would correspond to a different value of  $J_z$  for the teal and orange points. In this way, assuming the wrong coordinate system induces a phase dependence in the actions estimated for the star, which in the correct potential (in this example, the one with the correct midplane) should be phase independent.

This example uses an offset in z, but analogous effects occur from offsets in other coordinates, such as the distance to the Galactic center, or the LSR. A similar effect in which actions gain time dependence due to a time-varying potential was pointed out by Buist & Helmi (2015).

In reality one only ever measures the position and velocity of a star at a single instance in time. However, there are at least two possibilities for going beyond a single temporal snapshot of the phase-space distribution. If more than one star on the same or similar orbit could be identified (e.g., by identifying the remnants of a disrupted open cluster), then it would be possible to constrain the disk potential in analogy to how stellar streams are used to constrain the Galactic potential (e.g., Johnston et al. 1999; Ibata et al. 2001; Helmi 2004; Küpper et al. 2015; Sanderson et al. 2015; Laporte et al. 2019a). This would be challenging since, in principle, one would want to use the stellar actions or other conserved quantities, but as we discuss in this work they are subject to substantial errors. Another possibility would be to use chemical tagging to identify a disrupted open cluster (Freeman & Bland-Hawthorn 2002), but this may be difficult due to the large number of stars that are chemically indistinguishable though presumably born in different clusters (Ness et al. 2018). A second way to improve on a single temporal snapshot is to measure directly the accelerations of stars (Silverwood & Easther 2018). While this would allow a direct measurement of the aliasing effect in Figure 1, the observational challenges will likely limit this type of measurement to a small number of local stars for the near future.

## 2.2. Epicyclic Approximation

Before turning to numerical methods, we derive analytic expressions for the systematic error in the actions induced from offsets in the position (e.g., the midplane or Galactic center distance) or velocity (e.g., the LSR) of the assumed coordinate system's origin.

We use the epicyclic approximation, which assumes that the motion in the z- and R-components of the orbit are decoupled and follow simple harmonic motion about a circular and planar guiding orbit (Binney & Tremaine 2008, Section 3.2 and references therein). The radius of this orbit is referred to as the guiding radius  $R_g$ . This approximation is an excellent description of the thin disk and a good description of the thick disk in an axisymmetric potential that ignores the influence of the Galactic bar and spiral arms. We also make the assumption of a perfectly flat circular velocity curve with  $v_c(R) = v_c$ , a good approximation near the solar circle (e.g., McMillan 2017).

Under this approximation, we can write down the cylindrical components of the orbits as

$$R(t) = R_g + A_R \sin(\kappa t + \alpha)$$

$$\phi(t) = \Omega_c t$$

$$z(t) = A_z \sin(\nu t + \beta),$$
(2)

where  $\kappa$  and  $\nu$  are the radial/epicyclic and vertical frequencies,  $\Omega_c \equiv v_c/R_g$  is the orbital frequency of the guiding center,  $A_R$  and  $A_z$  are the amplitudes in the radial and vertical coordinates, and  $\alpha$  and  $\beta$  are the initial orbital phases. Similarly, the velocities of the orbit are given by

$$v_R(t) = \kappa A_R \cos(\kappa t + \alpha)$$

$$v_{\phi}(t) = v_c$$

$$v_{z}(t) = \nu A_z \cos(\nu t + \beta).$$
(3)

In this case, the azimuthal action is (Binney & Tremaine 2008, Section 3.5.3b)

$$J_{\phi} = R_{\sigma} \nu_{c},\tag{4}$$

and the radial and vertical actions are

$$J_R = E_R / \kappa$$

$$J_z = E_z / \nu,$$
(5)

where  $E_R$  and  $E_z$  are the energy per unit mass in the radial and vertical coordinates, respectively. Therefore,

$$J_{R} = \frac{v_{R}^{2} + \kappa^{2} (R - R_{g})^{2}}{2\kappa}$$

$$J_{z} = \frac{v_{z}^{2} + \nu^{2} z^{2}}{2\nu}.$$
(6)

Using Equations (2) and (3), we can simplify this:

$$J_{R} = \frac{\kappa A_{R}^{2}}{2} = \frac{v_{R,\text{max}}^{2}}{2\kappa}$$

$$J_{z} = \frac{\nu A_{z}^{2}}{2} = \frac{v_{z,\text{max}}^{2}}{2\nu},$$
(7)

where the last equality in each line comes from the fact that  $v_{R,\max} = \kappa A_R$  and  $v_{z,\max} = \nu A_z$ .

Notice that while the value for each of  $J_{\phi}$ ,  $J_{R}$ , and  $J_{z}$  is phase independent, the contribution from the kinetic and potential terms in Equation (6) is phase dependent. Now assume that the coordinates  $(R, z, v_{\phi}, v_{R}, v_{z})$  are offset by  $(\Delta R, \Delta z, \Delta v_{\phi}, \Delta v_{R}, \Delta v_{z})$ . We can then apply the standard propagation of errors formula to Equations (4) and (6) to determine the error in each of the actions. For  $J_{R}$ , the induced error is

$$\frac{\Delta J_R}{J_R} = \frac{2(R - R_g)}{A_R^2} \Delta R + \frac{2v_R}{v_{R,\text{max}}^2} \Delta v_R.$$
 (8)

For  $J_{\phi}$ , the induced error is

$$\frac{\Delta J_{\phi}}{J_{\phi}} = \frac{\Delta R}{R_{\sigma}} + \frac{\Delta \nu_{\phi}}{\nu_{c}}.$$
 (9)

For  $J_z$ , the induced error is

$$\frac{\Delta J_z}{J_z} = \frac{2z}{A_z^2} \Delta z + \frac{2v_z}{v_{z,\text{max}}^2} \Delta v_z.$$
 (10)

We have ignored second order contributions.

Since most of the time stars will be at maximum amplitude (i.e., turnaround) in both R and z, we can approximate the order of magnitude of the systematic error in the actions by

$$\frac{\Delta J_R}{J_R} = \frac{2\Delta R}{A_R}$$

$$\frac{\Delta J_\phi}{J_\phi} = \frac{\Delta R}{R_g} + \frac{\Delta v_\phi}{v_c}$$

$$\frac{\Delta J_z}{J_z} = \frac{2\Delta z}{A_z},$$
(11)

where we have again ignored second order terms.

Because the energies in the radial and vertical coordinates are related to the radial and vertical actions by a constant (Equation (5)), the fractional error in these two energies is the same as the actions. <sup>11</sup> The energy in the azimuthal coordinate can be readily computed ( $E_{\phi} = \frac{1}{2}v_{\phi}^2$ ). Using standard propagation of errors, we see that  $\Delta E_{\phi}/E_{\phi}$  and  $\Delta J_{\phi}/J_{\phi}$  (Equation (9)) differ by a  $\Delta R/R_g$  term. Since  $R_g \approx 8$  kpc, we expect this term to be negligible and we therefore conclude that

$$\frac{\Delta E}{E} \approx \frac{\Delta J_R}{J_R} + 2\frac{\Delta J_\phi}{J_\phi} + \frac{\Delta J_z}{J_z}.$$
 (12)

In the remainder of this section, we compare our analytic estimates of the effect of a midplane offset on actions against numerical calculations. A numerical evaluation of the effect of velocity offsets on actions is deferred to future work, as we discuss in Section 3.4.

#### 2.3. Numerical Methods

We now quantify the argument made in Section 2.1 using numerical computations of the actions for a range of orbits in a model Galactic potential. We compute actions as in Beane et al. (2018), using the code gala v0.3 to perform orbit integrations and conversion to action space (Price-Whelan 2017; Price-Whelan et al. 2019). To compute actions we use the torusmapping technique first presented by McGill & Binney (1990) and adapted by Sanders & Binney (2014) to calculate actions for an orbital time series starting from a phase-space position (x, v) and integrated in a potential  $\Phi$ . For our Galactic potential we use MWPotential, based on the Milky Way potential available in galpy (Bovy 2015), which includes a Hernquist bulge and nucleus (Hernquist 1990), a Miyamoto-Nagai disk (Miyamoto & Nagai 1975), and an NFW halo (Navarro et al. 1997), and is fit to empirically match some observations. We use the Dormand-Prince 8(5,3) integration scheme (Dormand & Prince 1980) with a timestep of 1 Myr and integrate for 5 Gyr, corresponding to  $\sim$ 20 orbits for a Sun-like star.

We assume the Sun is located at (8.2, 0, 0)kpc. None of our orbit integrations depend on the value of the LSR in this toy potential (though this is important when using real data, since the conversion from heliocentric to Galactocentric coordinates depends on the LSR). In this potential, we have that the circular velocity  $v_{\rm circ}$  is 231 km s<sup>-1</sup> at the solar circle.

Other methods for computing actions are used in the literature. For example, the Stäckel fudge method (Sanders & Binney 2016), which uses a single Stäckel potential (with analytic actions) to approximate the Galactic potential (de Zeeuw 1985; Binney 2012), was used in many recent works

<sup>11</sup> This ignores any potential error in the epicyclic and vertical frequencies.

Table 1

Names and Properties of the Three Orbits Considered in this Work, where  $z_{max}$  is the Maximum Height of the Orbit,  $\frac{1}{2}(R_{max}-R_{min})$  is the Magnitude of the Radial Excursions of the Orbit, and  $\kappa$  and  $\nu$  are the Radial/epicyclic and Vertical Frequencies of the Orbit

Name	Initial Position (kpc)	Initial Velocity (km s <sup>-1</sup> )	$J_R$ (kpc km s <sup>-1</sup> )	$J_{\phi}$ (kpc km s <sup>-1</sup> )	$J_z$ (kpc km s <sup>-1</sup> )	z <sub>max</sub> (kpc)	$\frac{1}{2}(R_{\text{max}} - R_{\text{min}})$ (kpc)	$\kappa (\mathrm{Myr}^{-1})$	$\nu$ (Myr <sup>-1</sup> )
thin-disk	(8, 0, 0)	(0, -190, 10)	40	-1500	0.69	0.12	1.3	0.049	0.093
thick-disk	(8, 0, 0)	(0, -190, 50)	33	-1500	23	0.85	1.2	0.048	0.061
halo	(8, 0, 0)	(0, -190, 190)	33	-1500	530	6.2	2.3	0.033	0.025

**Note.** In the epicyclic approximation,  $A_z = z_{\text{max}}$  and  $A_R = \frac{1}{2}(R_{\text{max}} - R_{\text{min}})$ .

exploring actions in the Galactic disk (e.g., Sanders & Das 2018; Ting & Rix 2018; Trick et al. 2019). For disk-like orbits, existing implementations of the Stäckel fudge method are of acceptable accuracy, but since we also consider halo-like orbits in this work (where the Stäckel fudge method is inaccurate) we choose to use orbit integration and torus mapping throughout (Sanders & Binney 2016).

#### 2.4. Quantification of the Midplane Effect

We now quantify how a systematic error in the Galacto-centric coordinate system induces phase dependence in the actions calculated from the observed position and velocity of a star. We consider three orbits in the model potential described in Section 2.3 that are typical of stars in the thin disk, thick disk, and halo. We summarize their initial positions in phase space, the actions computed by integrating their orbits in the correct potential, and other properties in Table 1. Each orbit, integrated without systematic coordinate errors, is plotted in Appendix A. We will refer to these orbits by their names (thin-disk, thick-disk, halo) henceforth.

We begin with thick-disk. Consider an observer who can measure the orbit's phase-space position at many different times (and hence different orbital phases), but does so using a coordinate system in which the midplane is systematically offset in height by  $100 \, \mathrm{pc}$  from its actual location. To model this we subtract the vector  $(0, \, 0, \, 100) \, \mathrm{pc}$  from each position in the orbit. This corresponds to an observer physically located at, e.g., the position  $(8, \, 0, \, 0) \, \mathrm{kpc}$  in the coordinate system of the true potential, but erroneously thinking they are located at  $(8, \, 0, \, 0.1) \, \mathrm{kpc}$ .

We consider the observer making a measurement, integrating an orbit, and computing actions every megayear using the prescription above. However, we specify the star's starting position using the systematically offset coordinate system. Essentially, we are shifting and then reintegrating at each point along the original orbit. The actions computed using the offset coordinate system for each phase-space starting point are shown for the first gigayear of the orbit in the upper panels of Figure 2. 12

We also perform the same procedure in the lower panels but assuming an x-component offset of 100 pc, i.e., subtracting the vector (100, 0, 0) pc. This is equivalent to a measurement error in the distance from the Sun to the Galactic center.

Figure 2 shows that the actions computed in the offset coordinate systems oscillate as a function of the time/orbital

phase at which the star's phase-space position is observed. This time dependence comes even though the observer is using the correctly constructed, best-fit, static, axisymmetric potential. The relative size of the phase variation in each action depends on the direction of the systematic offset as well as the true values of the actions (i.e., the type of orbit). In reality, we will have one measurement of the phase-space position to work with, in which case the determination of the orbital phase in R or z is degenerate with the degree of systematic offset in that coordinate (see Figure 1). In the following we therefore quote percentile ranges for the possible values computed for each action as a proxy for the effect of these systematic errors in the coordinate system.

For a systematic offset in z (upper panels), the 95th minus 5th percentiles are 2.2 and 6.2 kpc km s<sup>-1</sup> for  $J_R$  and  $J_z$ , respectively. As a fraction of the true values, these are 5.7% and 86%, respectively. The spread induced in  $J_\phi$  is negligible, as expected since  $J_\phi$  only depends on the x- and y-components of the position and velocity of the stars. It is worth pointing out that a 100 pc offset in an orbit with  $z_{\rm max} = 850$  pc—a 12% error—induced an 86% spread in the computation of  $J_z$ .

For a systematic offset in x (or distance to the Galactic center), the 95th minus 5th percentiles are 6.9, 47, and 0.71 kpc km s<sup>-1</sup> for  $J_R$ ,  $J_\phi$ , and  $J_z$ , respectively. These are fractionally 21%, 3.1%, and 3.1% in these actions, respectively, despite only a 1.2% error in the distance to the Galactic center.

In Figure 3, we plot a histogram of the values of  $J_z$  computed at different orbital phases for thick-disk (top panel) and thin-disk (bottom panel), assuming a z offset of 100 pc (as in the upper right panel of Figure 2). The true value is plotted as a vertical dashed line. The systematic error in  $J_z$  induced by a systematic offset in z is non-Gaussian and bimodal; neither of the modes is centered on the null value. In the case of thin-disk (bottom panel), we see that, in addition to the prior complications, the distribution is not even centered on the true value. This comes about when the midplane error is  $\gtrsim z_{\rm max}$ , where  $z_{\rm max}$  is the maximum height of the orbit (equivalent to  $A_z$  in the epicyclic approximation, see Section 2.2).

In Appendix C we plot the same histogram as in Figure 3, but for the distributions of  $J_R$  induced by a z offset (upper left panel of Figure 4) and the distributions of  $J_R$  and  $J_\phi$  errors induced by an x offset (lower left and lower center panels of Figure 4, respectively). We find similar error distributions as in Figure 3, with the exception that the computed  $J_R$  distribution induced by an x offset more closely resembles a Gaussian distribution.

We now suggest a heuristic explanation for the shape of Figure 3. Consider first the thick-disk (top panel), where the offset in z is much less than the  $z_{\rm max}$  of the orbit. The peaks in the distribution correspond to the turning points of the orbit

 $<sup>\</sup>overline{^{12}}$  Occasionally the numerical scheme fails and very large actions are reported by gala—we perform a  $4\sigma$  clip on each action to exclude such orbits, but this only excludes a total of 5 orbits out of the 1000 considered for Figure 2. Some numerical artifacts remain, but the vast majority of orbits are computed properly.

 $<sup>\</sup>overline{^{13}}$  In practice, however,  $J_{\phi}$  is computed as part of the torus-fitting method.

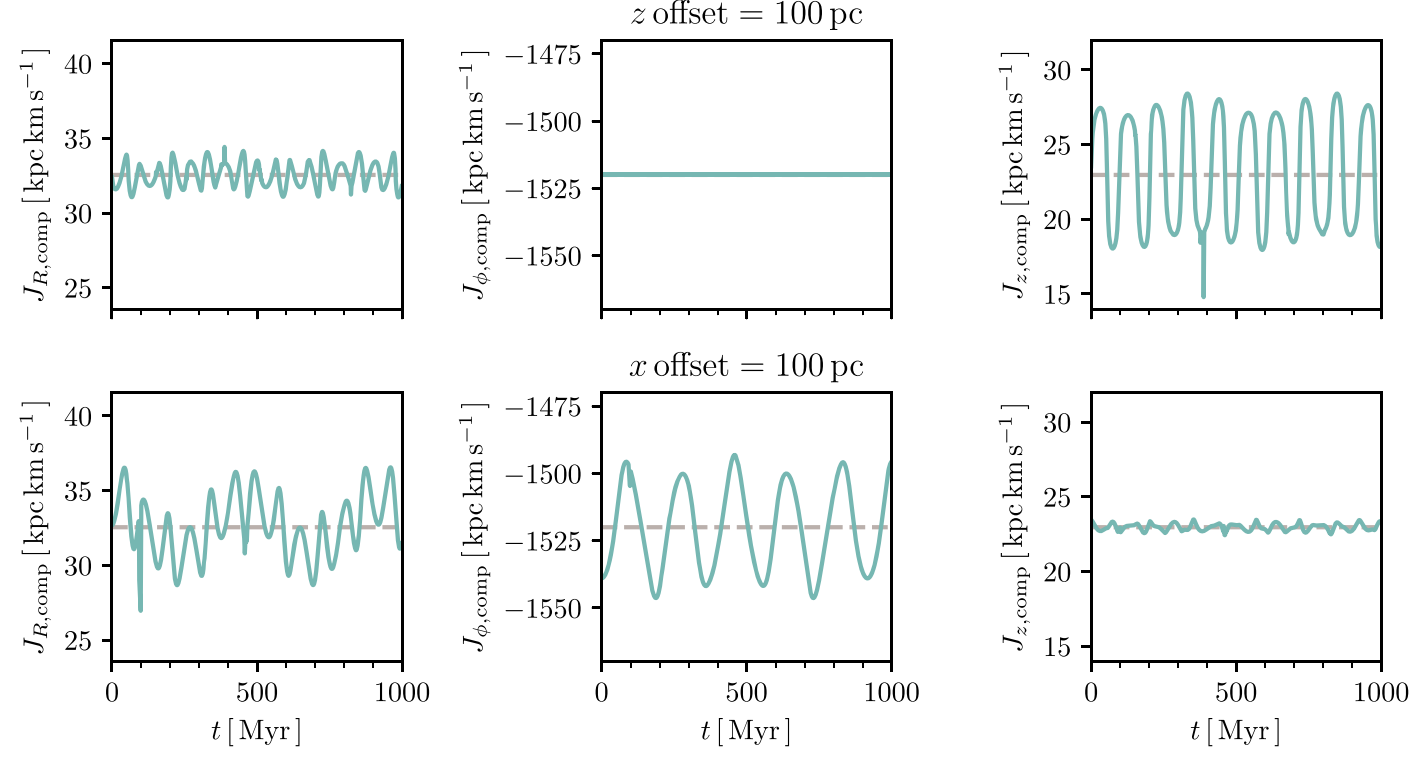


Figure 2. The artificial phase dependence in the computed actions with an error in the Galactocentric coordinate system. We consider here thick-disk, which has actions of  $(J_R, J_\phi, J_z) = (38, -1500, 7.0)$  kpc km s<sup>-1</sup> and  $z_{\text{max}} = 850$  pc (see Table 1). We integrate the orbit according to the procedure laid out in Section 2.3, and which we plot in Appendix A. Then, we subtract 100 pc from the z value (upper panels) or the x value (lower panels) of each position in the orbit, corresponding to an erroneous observer assuming a midplane (upper) or solar radius (lower) that is off by 100 pc. We then allow an observer to measure the orbit over 1 Gyr and perform the same orbit integration procedure at each timestep, and report the values of the actions, with the true values given as horizontal dashed lines. The computation of  $J_\phi$  is pristine to errors in z, with only numerical artifacts remaining. Only small errors are induced in  $J_R$ , with the middle 90% of values over the Gyr being within ~8% of the true  $J_R$ . As expected, large errors are induced in  $J_z$  with a 100 pc offset in z, with the middle 90% of values being within ~43% of the true  $J_z$ . The x offset induces uncertainties in  $J_R$ ,  $J_\phi$ , and  $J_z$  of ~21%, ~3%, and ~3%.

(or points of maximum vertical amplitude), where  $v_z \sim 0$  and where the star is on most of its orbit. This is why the distribution, which is calculated at evenly spaced time intervals, peaks at these values. For thin-disk (bottom panel), the offset in z is comparable to  $z_{\rm max}$ . Now, there will be some points in the orbit where  $v_z = 0$  and z = 0 (in the erroneous coordinate system). At these points, the computed  $J_z$  will vanish. The asymmetry and systematic offset then comes about because of the constraint that  $J_z \geqslant 0$ .

Gaussian summary statistics are clearly insufficient to describe the distribution shown in Figure 3. We therefore elect to measure this error by computing one half the 95th percentile minus the 5th percentile of the distribution of action values. We refer to this quantity as  $\Delta J_i$  for each action and plot it in Figure 3 as a horizontal arrow anchored on the true action value. Because of the bimodality of the error distribution, this quantity roughly measures the distance from the true action value to the peak of one of the modes. Furthermore, this bimodality also implies that  $\Delta J_i$  is not very sensitive to the exact percentiles used. This summary statistic does not reflect the bias induced when the midplane error is  $\gtrsim z_{\rm max}$ .

We now repeat the same procedure as in Figure 2 but for systematic offsets between 0 and 500 pc in the z- and x-components. In Figure 4, we report  $\Delta J_i/J_i$  for the three different fiducial orbits in Table 1. The upper panels of Figure 4

shows the spread induced in each action for an offset in the z-component. In the lower panels we consider offsets in the x-component (i.e., the solar radius). The left, center, and right columns show the fractional spread in the values computed for  $J_R$ ,  $J_{\phi}$ , and  $J_z$ , respectively.

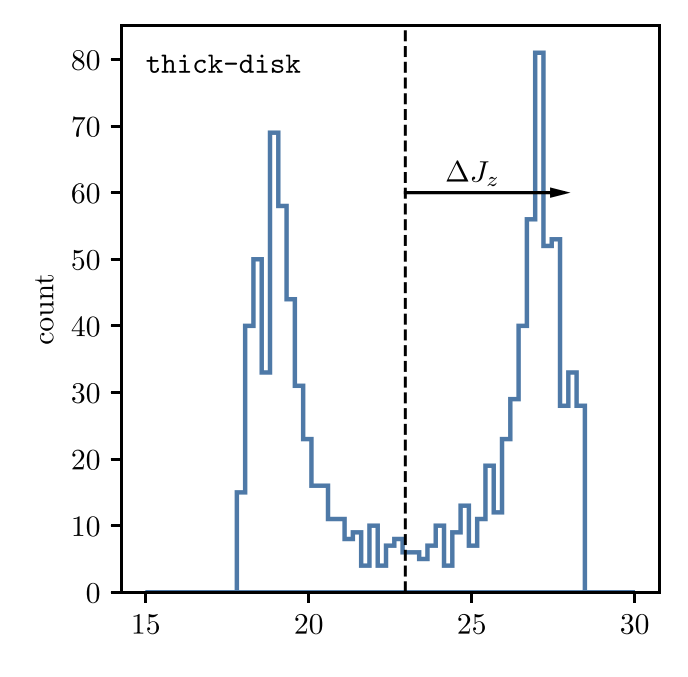
In the upper middle panel of Figure 4, there is essentially no spread in the determination of  $J_{\phi}$ . This is expected since  $J_{\phi}$  is independent of z and is thus unaffected by offsets in z, as discussed earlier. Indeed, the result we found in Figure 2 for thick-disk holds for all orbit types. This is also a demonstration of the robustness of the integration and action calculation methods we use.

The upper right panel of Figure 4 shows that the fractional error in  $J_z$  is more exaggerated for more planar (disk-like) orbits. For thin-disk, a systematic offset of 15 pc in the z-coordinate results in a 25% deviation in  $J_z$ , while a 120 pc offset results in the same deviation for thick-disk. We find that halo is relatively insensitive to errors in the midplane, with only  $\sim\!15\%$  error in  $J_z$  out to an offset of 500 pc.

For the offset in the solar radius (lower panels), the error is largest for  $J_R$ , with some deviations resulting in  $J_{\phi}$  and relatively small deviations in  $J_z$ . In the lower center and lower right panels all three lines nearly overlap.

In each panel of Figure 4, where relevant, we include the estimation of the action errors derived under the epicyclic approximation from Equation (11), with  $\Delta v_{\phi} = 0$ , as dashed lines in the color of each orbit. This equation is relevant since during most of the orbit the star will be close to maximum radial and vertical amplitude. Note that we consider an error in the *x*-coordinate  $\Delta x$ ,

<sup>&</sup>lt;sup>14</sup> This argument is similar to ones given in cosmology for why gravity produces non-Gaussianity in the density field, since the density cannot become negative but it can grow arbitrarily large.



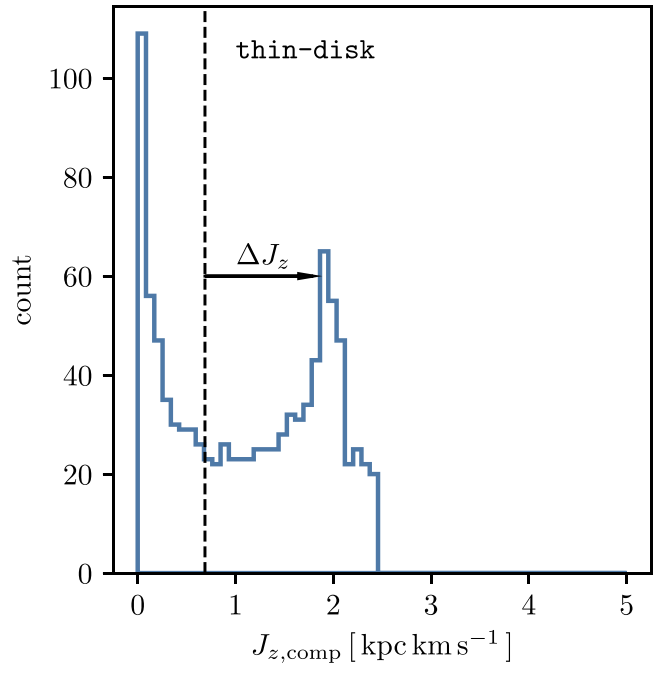


Figure 3. A histogram of the computed values of  $J_z$  at different orbital phases for thick-disk (top panel) and thin-disk (bottom panel) assuming a z offset of 100 pc. One can see that if the observed z values have a bias (from, e.g., an incorrectly computed midplane), then the induced error distribution in  $J_z$  is decidedly non-Gaussian. Therefore, any sort of error propagation must take this into account. A heuristic explanation for the shape of each panel is given in the text. We also plot one half the 95th percentile minus the 5th percentile of each distribution as a horizontal arrow anchored on the true  $J_z$  value. We call this  $\Delta J_z$  and will use it (along with the similarly defined  $\Delta J_R$  and  $\Delta J_\phi$ ) to empirically describe the error distribution. We see that  $\Delta J_z$  roughly corresponds to the distance from the true  $J_z$  value to one of the modes of the distribution of computed  $J_z$  values. Similar plots for  $J_R$  induced by a z offset and  $J_R$  and  $J_\phi$  induced by an x offset are given in Appendix C.

which is not exactly the same as  $\Delta R$ . For observations of stars close to us, we have that  $\Delta x \sim \Delta R$ , but for the experiment performed in this section we consider observations of the star throughout its entire orbit. This introduces a factor of  $2/\pi$  when converting from  $\Delta x$  to  $\Delta R$ , which we derive in Appendix B.

The epicyclic approximation is a good predictor of  $\Delta J_z$ , even for halo. It performs similarly for  $\Delta J_R$ , now underpredicting for halo and slightly overpredicting for thin-disk. Note that for the particular orbits we chose, thin-disk has slightly larger  $A_R$  than thick-disk, and so we actually expect the epicyclic approximation to perform slightly worse for thin-disk in this case. The epicyclic approximation underpredicts  $\Delta J_\phi$  for all orbits.

To further understand the effect of the midplane error, we also plot the fractional error in  $J_z$  as a function of  $J_z$  for z offsets of 10, 50, and 100 pc (orange, teal, and green, respectively) in Figure 5. For each orbit, we set the initial position to be (8, 0, 0)kpc and the initial velocity to be  $(0, -190, v_z) \, \mathrm{km \, s^{-1}}$ , where we vary  $v_z$ . For a thin-disk-like orbit ( $J_z \sim 0.7 \, \mathrm{kpc \, km \, s^{-1}}$ ), even a 10 pc offset in z is enough to induce a  $\sim 20\%$  error in  $J_z$ . For larger values of  $J_z$ , the fractional errors are suppressed, but the induced error can still be large depending on how great the z offset is. We also plot the epicylic prediction for  $\Delta J_z/J_z$  from Equation (11) as dashed lines for each z offset. We find that the epicyclic approximation matches the numerical estimate quite well.

#### 3. Azimuthal Midplane Variations

The stellar midplane of the Galaxy should vary as a function of azimuth and Galactocentric radius due to small, local variations in the stellar density. Hints of this variation as a function of Galactocentric radius have been noted through their impact on the stellar velocity distribution pre-*Gaia* by Widrow et al. (2012), Carlin et al. (2013), and Williams et al. (2013) and recently post-*Gaia* by Friske & Schönrich (2019). As pointed out by, e.g., Goodman et al. (2014) and Anderson et al. (2019), among many others, the gas distribution in the Galaxy also shows significant density variation across the disk.

The local Galactocentric coordinate system is defined based on the location of the Sun relative to the midplane. Extending this coordinate system to a global one therefore introduces systematic errors in the *z*-components of stellar positions. As discussed in Section 2, this systematic error introduces errors in integrating orbits and computing actions.

We specifically consider *azimuthal* variations in the midplane at the solar circle, as defined by the stellar mass density. Since, to our knowledge, there are no direct empirical measurements of these variations in the Milky Way, we use example simulations from two classes of simulations to estimate the size of this effect.

One set are three zoom-in, cosmological hydrodynamical simulations of isolated Milky Way-mass galaxies from the FIRE collaboration, described briefly in Section 3.1. These include stars, gas, and dark matter in a fully cosmological setting but are not tailored to specific properties of the Milky Way (such as the scale height or scale length, or the details of the accretion history). We use these simulations to span the range of possibilities for azimuthal midplane variations.

The other set of simulations are isolated *N*-body simulations of interactions between the Milky Way and a Sagittarius-like dwarf galaxy, described briefly in Section 3.2. These include dark matter and stars and are tailored to existing measurements of the structure of the Milky Way's disk and of the orbit and properties of the Sagittarius dwarf galaxy. Comparing the azimuthal midplane variations in the host galaxy of these simulations before and after the interaction with the Sagittarius-like object gives an idea of the effect of one minor merger

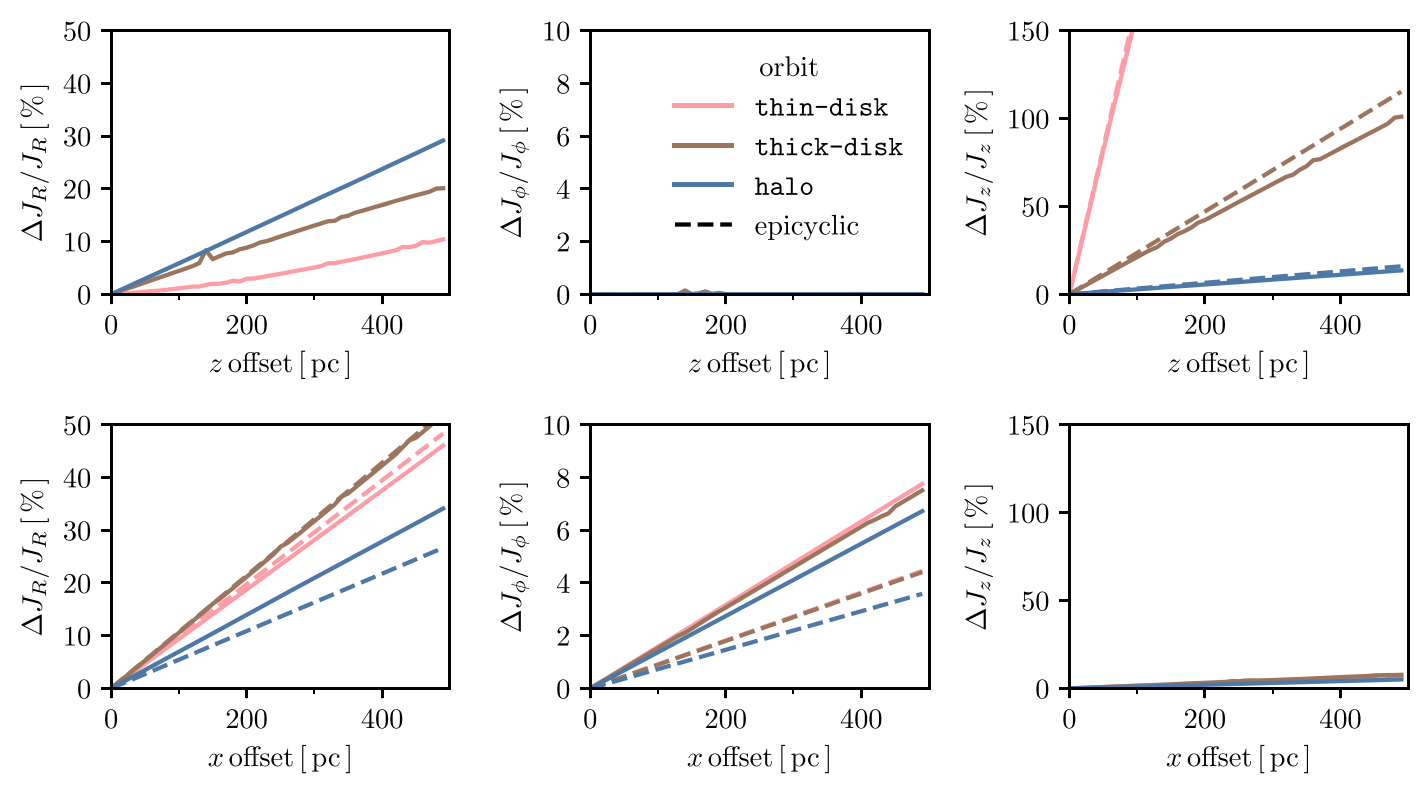


Figure 4. We report the fractional error in each action  $J_i$  induced by coordinate system offsets for thin-disk, thick-disk, and halo (Table 1). The error  $(\Delta J_i)$  is computed as one half the 95th minus 5th percentile of the distribution of computed action values. See discussion in the text and Figure 3 for the justification in using this to measure the magnitude of the induced error. The left, center, and right panels show the result for  $J_R$ ,  $J_{\phi}$ , and  $J_z$ , respectively. The upper panels consider an offset in z and the lower panels consider an offset in x (equivalently, an offset in the solar radius). In some panels, we also plot as dashed lines the epicyclic prediction of the induced action error (Equation (11)). In the epicyclic approximation, a z offset only induces an error in  $J_z$ —for all three orbits the epicyclic approximation is a good description of the  $J_z$  error. An z offset induces an error in  $J_R$  and  $J_{\phi}$ . The error in  $J_R$  is somewhat well described for thin-disk and thick-disk, and a poor description for halo. For  $J_{\phi}$ , the epicyclic approximation is not a good description for any orbit.

whose properties are relatively well measured. Azimuthal variations of the mean vertical height of stars has been explicitly pointed out in a different simulation of a Sagittarius-like encounter by Gómez et al. (2013).

#### 3.1. Description of FIRE Simulations

The FIRE cosmological hydrodynamic simulations (Hopkins et al. 2014, 2018) use the zoom-in technique (e.g., Katz & White 1993; Oñorbe et al. 2014) to model the formation of a small group of galaxies at high resolution in a full cosmological context. Feedback from supernovae, stellar winds, and radiation from massive stars is implemented at the scale of star-forming regions following stellar population synthesis models, generating galactic winds self-consistently (Muratov et al. 2015; Anglés-Alcázar et al. 2017) while reproducing many observed galaxy properties, including stellar masses, star formation histories, metallicities, and morphologies and kinematics of thin and thick disks (Hopkins et al. 2014; Ma et al. 2016, 2017; Wetzel et al. 2016; Garrison-Kimmel et al. 2018; Hopkins et al. 2018).

For this work, we focus on the three Milky Way-mass zoomins considered in Sanderson et al. (2018), which were simulated as part of the *Latte* suite and show broad agreement of many of their global properties with observations of the Milky Way (Wetzel et al. 2016; Garrison-Kimmel et al. 2018). The  $z_r = 0$  snapshots of these three simulations, The

snapshots of these three simulations at cosmological redshift  $z_r = 0$ , named m12i, m12f, and m12m, are publicly available alongside associated mock *Gaia* DR2 catalogs generated from them. <sup>16</sup>

These simulations contain dark matter particles of mass  $\sim 35,000\,M_\odot$ , gas particles of mass  $\sim 7000-20,000\,M_\odot$ , and star particles of mass  $\sim 5000-7000\,M_\odot$ , with the lower end coming from stellar evolution (Sanderson et al. 2018). Softening lengths for dark matter and star particles are fixed at 112 and 11.2 pc, respectively. The gas softening length is adaptive, but at  $z_r=0$  the median softening length for cold ( $T<100\,\mathrm{K}$ ) gas particles around roughly solar positions (with galactocentric cylindrical radii within 0.5 kpc of 8.2 kpc and  $|z|<1\,\mathrm{kpc}$ ) is 53.4, 57.2, and 60.1 pc for m12i, m12f, and m12m, respectively. These values are summarized in Table 2, along with measurements of the stellar and gas disk scale heights.

The softening lengths used in the simulations can affect the ability to resolve the very thinnest planar structures, which in turn can affect how much the density-based midplane varies as a function of azimuth. The Milky Way's dense, star-forming gas disk is thought to have a scale height of about 40 pc, on the order of the cold gas softening length (Anderson et al. 2019). The thin stellar disk has a scale height of about 300 pc,  $\sim$ 30 times the stellar softening length (Jurić et al. 2008). We therefore expect that resolution effects are still affecting the

 $<sup>\</sup>overline{^{15}}$  In this work, to avoid confusion with the vertical height z, we refer to cosmological redshift as  $z_r$ .

<sup>16</sup> http://ananke.hub.yt

<sup>17</sup> This is 2.8 times the often-quoted Plummer equivalent.

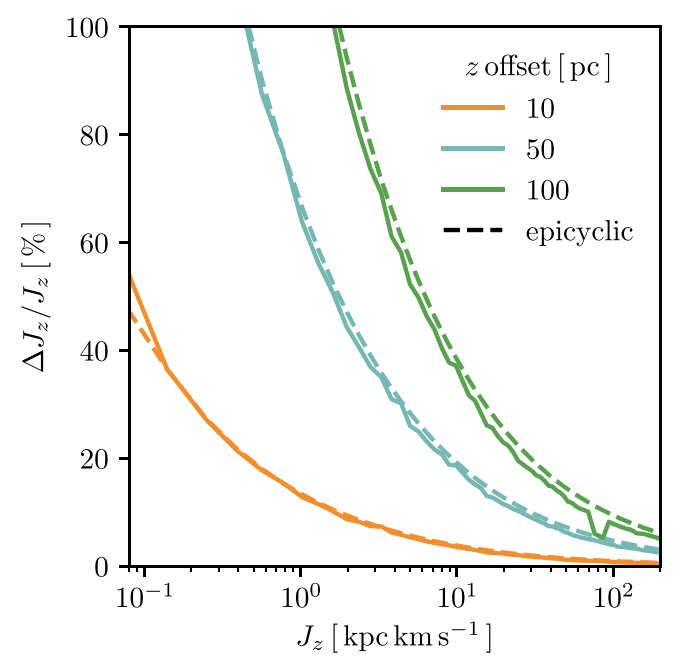


Figure 5. The fractional error in  $J_z$  as a function of  $J_z$  for a few different offsets in z. All orbits have the same initial position of (8,0,0)kpc and velocity  $(0,-190,\nu_z)$  km s<sup>-1</sup>, where we vary  $\nu_z$ . (One can recover thin-disk, thick-disk, and halo by setting  $\nu_z=10$ , 50, and 190, respectively, giving  $J_z\simeq 0.7$ , 20, and 500 kpc km s<sup>-1</sup> (see Table 1).) We show this for a z offset of 10, 50, and 100 pc (orange, teal, and green, respectively). As before, the error  $(\Delta J_z)$  is one half the 95th minus 5th percentile of the distribution of computed  $J_z$  values over the course of the orbit. There are large errors for thin-disk-like orbits  $(J_z\sim 0.7 \text{ kpc km s}^{-1})$ , even for a small midplane offset of 10 pc. As dashed lines in each color we also plot the prediction for  $\Delta J_z/J_z$  from the epicyclic approximation (Equation (11)), which shows excellent agreement with the numerically computed values.

scale heights of these components in the simulations, especially the cold gas. Indeed, the stellar scale heights of the simulated galaxies are equal to or larger than the Milky Way's, while the gas scale heights are significantly larger (although the proper basis comparison is less clear in the case of the gas; the quoted value for the Milky Way comes from studies of high-mass star-forming regions). The midplanes defined by gas and stars can be tilted with respect to one another as well, precluding extending the precision of the gas midplane definition to the stellar component.

Cosmological simulations of Milky Way-mass galaxies are not perfect representations of the true Milky Way in other ways as well, as discussed in Sanderson et al. (2018). The failure of cosmological simulations to exactly reproduce the Milky Way is not necessarily due to limitations of the numerical model. Candidate Milky Way-like galaxies are chosen solely on their mass and isolation, for which there are a wide variety of possible galaxies with qualitatively different properties. For example, the velocity structure of m12i is closer to M31's than the Milky Way's (S. Loebman et al. 2019, in preparation).

However, in this work we are most interested in the global properties of the potential, and specifically in deviations from axisymmetry. From this perspective, the simulated galaxies are actually *more* axisymmetric than we might expect of the Milky Way. While they have prominent spiral arms, none has as strong a bar as the Milky Way does at present day, and none has a nearby companion like the Large Magellanic Cloud. One of the three we consider (m12f) does have an ongoing interaction with a satellite galaxy similar in mass to Sagittarius,

which has punched through the Galactic disk outside the solar circle, leaving behind some of its stars and inducing warping in the disk

In this work, we take the galactocentric coordinate system described in Section 3 of Sanderson et al. (2018) as our fiducial coordinate system for each galaxy. In short, the center of the galaxy is found iteratively. The center of mass velocity is then determined by all star particles within 15 kpc of this center. The galaxy is then rotated onto a principal axis frame determined by stars younger than 1 Gyr inside of the fiducial solar radius  $R_0 = 8.2$  kpc, such that the disk plane is the x-y plane.

## 3.2. Description of Milky Way-Sagittarius Interaction Simulation

In addition to the cosmological zoom-ins, we will also briefly consider results from a live *N*-body simulation of a Sagittarius-like encounter. This simulation offers us the ability to see how the midplane varies in a more controlled environment. The simulation is described by Laporte et al. (2018), but we briefly summarize the most relevant details here.

For the Milky Way, the dark halo is modeled as a Hernquist sphere of mass  $10^{12}\,M_\odot$  and scale length of 52 kpc (Hernquist 1990), the disk is modeled as an exponential disk with a scale radius of 3.5 kpc, scale height 0.53 kpc, and mass  $6\times10^{10}\,M_\odot$ , and the bulge as a Hernquist sphere of mass  $10^{10}\,M_\odot$  and scale length 0.7 kpc. The Sagittarius dwarf is modeled with two components: a dark matter Hernquist sphere of mass  $8\times10^{10}\,M_\odot$  and scale length 8 kpc, and a stellar component modeled as a Hernquist sphere of mass  $6.4\times10^{8}\,M_\odot$  and scale length 0.85 kpc. All components are realized with distributions of live *N*-body particles; the Milky Way and Sagittarius are each initialized to be in equilibrium in isolation.

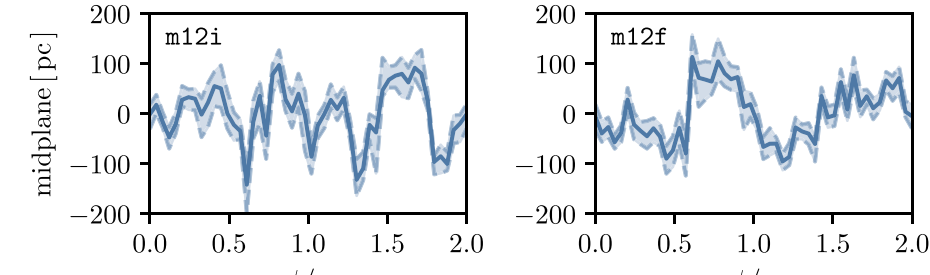
The mass resolution of the simulation is  $2.6 \times 10^4$ ,  $1.2 \times 10^4$ , and  $1.0 \times 10^4 \, M_\odot$  for the dark matter, disk, and bulge components, respectively. For the disk and bulge components, a softening length of 30 pc is used, whereas for the halo a softening length of 60 pc is used. For Sagittarius, the softening length for the dark matter and the stars is 60 and 40 pc, respectively.

The fiducial coordinate system for these *N*-body simulations is the rest frame of the aligned host galaxy at the beginning of the simulation.

## 3.3. The Local Midplane

Using the two sets of simulations, we determine the local midplane as a function of azimuth at the solar circle that an observer might measure if they were situated in each of these galaxies. Starting from the coordinate system described in the previous section, which is aligned so that the z-coordinate is approximately perpendicular to the disk plane at the solar circle, we place our imaginary observer at z = 0 and a galactocentric cylindrical radius of 8.2 kpc and vary the azimuth between  $0 < \phi < 2\pi$ . At equally spaced values of  $\phi$ we then compute the median z for stars within a cylinder of radius 0.5 kpc and height 1 kpc perpendicular to the fiducial disk and centered on it. We choose to use 50 bins in azimuth, sufficiently few that no cylinder shares stars with its neighbors. We then redefine the new midplane of the cylinder to be the median z, reselect stars, and iterate until the median z value converges. We find that only 10 iterations of this procedure are necessary for convergence. The resulting median z is taken to

2.0



 $\phi/\pi$ Figure 6. The local midplane determined at the fiducial solar circle ( $R_0 = 8.2 \text{ kpc}$ ) for the three FIRE galaxies m12i, m12f, and m12m (left, center, and right panels) as a function of azimuthal angle, at cosmological redshift  $z_r = 0$ . The local midplane is determined at a position  $\phi$  by taking the median height of all stars within R = 0.5 kpc and z = 1 kpc (in cylindrical coordinates). In order to allow for the possibility that the fiducial galactocentric coordinate system is incorrect, we subtract the best-fit sine curve from each panel. We then bootstrap resample 1000 times to determine 1  $\sigma$  error bars, which we report as dashed lines.

 Table 2

 Stellar and Gas Disk Scale Heights of the Milky Way and the FIRE Galaxies Considered in This Work (Described in Section 3.1)

Galaxy	Cold <sup>a</sup> Gas Disk Scale Height (pc)	Thin Disk Scale Height (pc)	Thick Disk Scale Height (pc)	Cold <sup>a</sup> Gas Softening Length (pc)	Stellar Softening Length (pc)
Milky Way <sup>b</sup>	40	300	900	•••	
m12i <sup>c</sup>	800 <sup>d</sup>	480	2000	53.4	11.2
m12f°	360	440	1280	57.2	11.2
m12m <sup>c</sup>	250	290	1030	60.1	11.2

**Notes.** For comparison, we also give the median softening lengths for the FIRE galaxies, computed for cold gas (T < 1000 K) and stars with  $|R - R_0| < 0.5 \text{ kpc}$  and |z| < 1 kpc. We have assumed that  $R_0 = 8.2 \text{ kpc}$ .

be what our observer would measure as the local galactic midplane at each  $\phi$ .

This procedure assumes perfect density estimation, and therefore perfect corrections for extinction within the cylinder defining the "solar neighborhood." Imperfect extinction correction is likely to increase the amplitude of the estimated fluctuations in *z*.

To account for the effect of particle noise, we bootstrap resample stars within a cylinder of height 2 kpc and the same radius 1000 times and determine the 1  $\sigma$  error bars by repeating the midplane determination with that reselection.

To allow for potential small inaccuracies in the determination of the original fiducial coordinate system, we also subtract the best-fit curve of the form

$$A\sin\left(\phi + B\right) + C\tag{13}$$

from the midplane as a function of azimuth to account for an overall tilt of the midplane (a simplified version of the strategy described in Anderson et al. 2019). For simulations (m12i, m12f, m12m), the best-fit values are A=(-170,45,8.8) pc, B=(38,-5.0,1.8) deg, and C=(-69,19,-18) pc. For the assumed solar radius of 8.2 kpc, we can approximate the angle offset  $\Delta\theta$  for the z-axis from the values of A. We find for the same simulations  $\Delta\theta=(1.15,0.31,0.062)$  deg. These angle offsets are consistent with the values given in Sanderson et al. (2018) for the difference between the z-axis as defined by the gas and stars.

Figure 6 shows the relative z location of the inferred midplane an observer would determine as a function of azimuth

for each galaxy, using their local solar neighborhood (the cylinder defined above). The  $1\sigma$  error from the bootstrap procedure is shown as the dashed-line error bars. The middle 90% of midplane values across the solar circle spans (190, 160, 84) pc for these simulations. In two of the three cases the midplane therefore varies by more than  $\pm 100$  pc depending on the azimuth along the solar circle; in the third (m12m, which has the thinnest "thin disk" of stars, but the largest stellar mass) the variation is closer to  $\pm 50$  pc.

200

100

-100

-200

0

0.0

m12m

0.5

1.0

1.5

We compute the same midplane variation in Figure 7, but for four successive time steps of the live *N*-body simulation of a Sagittarius encounter (Laporte et al. 2018). Again we have subtracted a best-fit curve of the form given in Equation (13), with the values at times (2.0, 4.0, 6.0, 6.9) Gyr being A = (9.5, 2.5, -210, -390) pc, B = (0.074, 0.039, -36, -57) deg, and C = (2.6, -7.8, -65, -53) pc. The middle 90% of midplane values across the solar circle spans (49, 62, 140, 120) pc.

These values for the midplane variation are consistent with the azimuthal midplane variations seen by Gómez et al. (2013). However, they only saw significant variations in their Heavy but not their Light Sagittarius model (virial masses of  $10^{11}\,M_{\odot}$  and  $\sim 3 \times 10^{10}\,M_{\odot}$ , respectively). The model we used (L2 from Laporte et al. 2018) has a virial mass of  $6 \times 10^{10}\,M_{\odot}$ , intermediate between their two models.

In the upper panels, we see that the midplane is relatively flat in the inner galaxy, but additional encounters drive strong midplane variation. In the lower left panel, we see a strong m=2 mode develop, consistent with the R=8 kpc panel of Figure 17 in Laporte et al. (2018) (m=0 and m=1 modes are stronger, but these are removed in our sine-curve subtraction). The lower right

 $<sup>^{\</sup>rm a}$  T < 100 K.

<sup>&</sup>lt;sup>b</sup> Jurić et al. (2008), Bland-Hawthorn & Gerhard (2016).

<sup>&</sup>lt;sup>c</sup> Sanderson et al. (2018).

d The azimuthally averaged gas vertical density profile in m12i is nearly constant to this height, though individual regions show smaller scale heights and dense clouds.

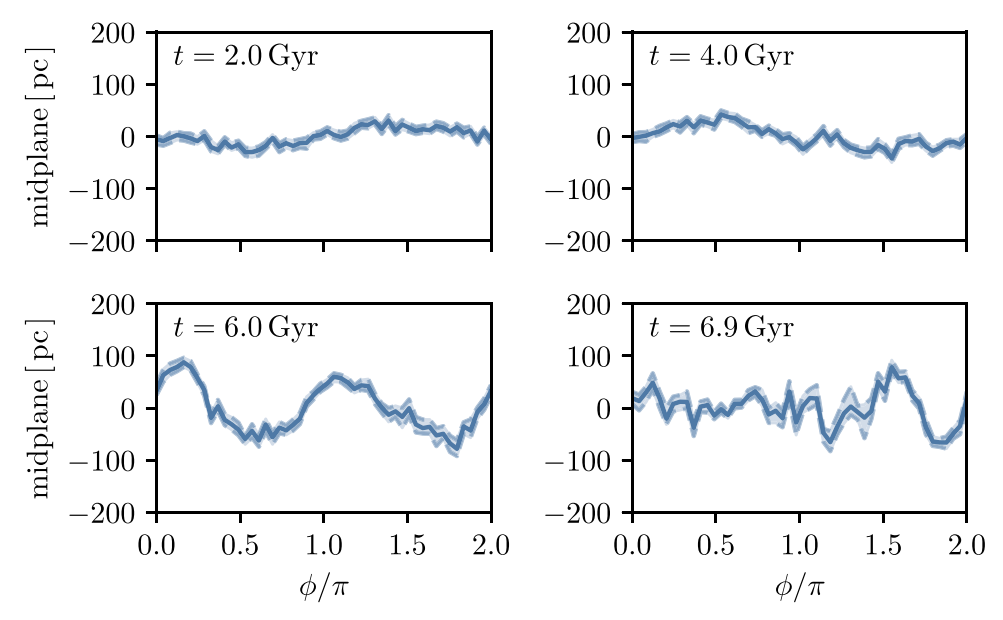


**Figure 7.** The local midplane determined at the fiducial solar circle ( $R_0 = 8.2 \text{ kpc}$ ) for four different time steps from a live *N*-body simulation of a Sagittarius encounter with the Milky Way (Laporte et al. 2018). As before, we have subtracted the best-fit sine curve to account for inaccuracies in the galactocentric coordinate system. Error bars are calculated as in Figure 6. The upper panels show the midplane as a function of azimuth before the first encounter near the solar circle at t = 2.0 Gyr and t = 4.0 Gyr, with an encounter happening close to the solar circle near t = 6.0 Gyr. The fact that the t = 6.9 Gyr panel, which shows the midplane variation after some relaxation, looks qualitatively similar to the panels from the FIRE simulations (Figure 6) is evidence that midplane variations are generated, in part, by mergers.

panel, which shows the galaxy at t = 6.9 Gyr when some relaxation has occurred, is qualitatively similar to the midplane variations we saw in the FIRE simulations (Figure 6), evidence that they are at least partially driven by mergers.

#### 3.4. Velocity Variations

We also expect that the LSR should vary as a function of azimuth. We perform this calculation in Appendix D to estimate the components of the LSR as a function of azimuth, but performing a best-fit subtraction to correct for misalignment of the original coordinate system (as in the previous section) is more involved. Since we find that the variation in the LSR is less pronounced than for the midplane, and since offsets in velocity only contribute to second order to  $\Delta J_R$  and  $\Delta J_z$  when a star is at maximum amplitude in R or z (where the majority of the orbit is, see Section 2.2), we defer this calculation to future work.

## 4. Discussion

We have used high-resolution simulations to illustrate why we expect the local midplane defined by stellar density to vary with azimuth by up to  $\pm 100$  pc as a natural consequence of the non-axisymmetry of the Galactic disk at small scales. While this is not in itself surprising or new, we have also argued that the discrepancy between our local midplane and that of distant stars introduces a systematic error in the z-component when converting from heliocentric to Galactocentric coordinates. This systematic error introduces a non-Gaussian error in the vertical action,  $J_z$ , when starting from the present-day positions and velocities of stars as measured by, e.g., Gaia.

These systematic errors are most important for stars on thin disk-like orbits, where they can be large enough to yield actions representative of orbits in the thick disk. This effect is entirely due to the extension of a local to a global coordinate system, and is separate from real diffusion in stellar integrals of motion

caused by interactions with these same deviations from axisymmetry, such as resonant perturbation by spiral arms or scattering from molecular clouds (Sellwood 2014).

## 4.1. Estimates of Milky Way Midplane Offsets

Systematic variations in  $v_z$  and number density were first noted as asymmetries in the local velocity distribution toward the North and South Galactic Caps from the radial velocity surveys of the SDSS (Widrow et al. 2012) and RAdial Velocity Experiment (Williams et al. 2013). Subsequently, Carlin et al. (2013) pointed out suggestions of an oscillation in average vertical velocities of order  $5 \, \mathrm{km \, s^{-1}}$  on roughly kiloparsec scales looking toward the Galactic anticenter.

Work by the *Gaia* collaboration confirmed these preliminary results on the velocity and spatial scales of oscillation with clear spatial maps made using DR2 data of median  $v_z$  over a significant Galactic volume (*Gaia* Collaboration et al. 2018b; Friske & Schönrich 2019), which can be explained with models of Sagittarius-like encounters (Gómez et al. 2013; Laporte et al. 2018, 2019b). We also see in the FIRE simulation that the vertical velocity variation as a function of azimuth is  $\sim 5-10 \,\mathrm{km \, s^{-1}}$  (Figure 10), consistent with these observations.

The vertical frequency of thin-disk and thick-disk are  $\sim 0.09$  and  $\sim 0.06 \, \mathrm{Myr^{-1}}$ , respectively (Table 1). By dimensional analysis, and assuming a vertical velocity variation of 5–10 km s<sup>-1</sup>, we therefore expect the midplane offsets to be  $\sim 57-170 \, \mathrm{pc}$ . We stress that this is a rough calculation.

Three-dimensional dust maps also offer a view into the expected variation of the stellar disk, since dust should trace regions of massive star formation. Figure 9 of Chen et al. (2019), Figure 1 of Leike & Enßlin (2019), and Figure 2 of Green et al. (2019) all show that the midplane varies by  $\sim\!10^\circ$  at a distance of  $\sim\!0.75$  kpc, corresponding to a physical vertical variation of  $\sim\!130$  pc.

Already we see evidence in the data from velocities and dust maps for midplane offsets on the order of what we saw in both sets of simulations.

#### 4.2. Uncertainties in the Solar Position and Velocity

Uncertainties in measurements of the position and velocity of the Sun relative to the Galactic center can also contribute to systematic error in the actions, since converting from heliocentric to Galactocentric coordinates relies on these measurements. Therefore, errors in their values will induce a systematic offset in the Galactocentric phase-space position of any observed star. Considerable effort has been placed on each of these measurements, but uncertainties remain, and detailed modeling across the disk—particularly for dynamically cold stars—may have to take them into account. Here we briefly review the current measurements of the four relevant quantities, their uncertainties, and the implications for the calculation of actions.

#### 4.2.1. Galactic Center Position

First, one must define the center of the Galaxy. This is usually taken to be the location of the central supermassive black hole, Sagittarius A\* (Sgr A\*, e.g., Reid & Brunthaler 2004). From stellar motions near Sgr A\*, the distance from the Sun to Sgr A\*,  $R_0$ , can be precisely measured (Gillessen et al. 2009; Gravity Collaboration et al. 2018). A recent measurement using near-infrared interferometry places  $R_0$  at  $8.178 \pm 0.035$  kpc (Abuter et al. 2019), or a 0.4% uncertainty.

However, the location of Sgr A\* may not be equivalent to the location of the dynamical Galactic center, the point in threedimensional space about which the stars in the solar neighborhood are orbiting. This assumption, although sensible and frequently made, has not yet been justified.

If the dynamical Galactic center is offset from Sgr A\* by 100 pc, only a 1.2% difference, then this induces a  $\sim$ 15% error in  $J_R$  for the disk-like orbits we considered (see Section 2.4). The reason such a large error in  $J_R$  can be generated by a small error in  $R_0$  can be understood from the epicyclic approximation (Equation (11)), which states that  $\Delta J_R/J_R=2\Delta R/A_R$ . The fractional error in  $J_R$  is related to the error in  $R_0$  as a fraction of the radial amplitude of the orbit, which is much smaller than  $R_0$  ( $\sim$ 1.2 kpc for thin-disk and thick-disk). This also implies the very precise 0.4% measurement of  $R_0$  still translates to a  $\sim$ 6% uncertainty in  $J_R$ .

The assumption that the dynamical Galactic center and Sgr A\* are colocated is tested in any construction of a dynamical model where  $R_0$  is a free parameter. For example, Küpper et al. (2015) measured  $R_0$  while modeling the dynamics of the stream Palomar 5. Many other dynamical measurements of  $R_0$  have been made (Bland-Hawthorn & Gerhard 2016 summarize many pre-*Gaia* results), but none have yet achieved a precision comparable to that of the distance to Sgr A\*.

We did not consider in this work the effect of the angular position of the dynamical Galactic center being offset from Sgr A\*.

#### 4.2.2. Galactic Orientation

Second, one must define the angular orientation of the Galaxy. This was defined in 1958 by the IAU subcomission 33b (Blaauw et al. 1960) by defining the coordinates of the Galactic center in B1950 coordinates as (17:42:26.6, -28:55:00) and the North Galactic pole as (12:49:00, +27:24:00). These two quantities,

together with  $R_0$ , define the orientation of the Galactic plane. However, there is growing evidence that the stellar midplane is tilted relative to this coordinate system (Goodman et al. 2014; Bland-Hawthorn & Gerhard 2016), though not the H II midplane (Anderson et al. 2019).

This tilt will contribute a systematic offset in z, with the exact magnitude depending on the position of the observed star. For instance, Goodman et al. (2014) quote a  $\sim$ 0°.4 tilt at 3.1 kpc, corresponding to a vertical height of  $\sim$ 22 pc. This corresponds to a 37% error in  $J_z$  for thin-disk and a 5% error for thick-disk.

#### 4.2.3. Solar Height

Third, one must define the Sun's vertical distance from the Galactic midplane, which can be determined by identifying where the stellar density and velocities reach a maximum (effectively the median height of all disk stars). The solar height is usually taken to be  $\sim 25$  pc (Chen et al. 2001), with a more recent measurement from Gaia DR2 placing it at  $20.8 \pm 0.3$  pc (Bennett & Bovy 2019). Another strategy is to use the cold gas or H II regions in the disk to define the Galactic midplane, leading to slightly different values (by  $\sim$ 5 pc) for the Sun's relative height (e.g., Anderson et al. 2019). A pre-Gaia review of these measurements is given by Bland-Hawthorn & Gerhard (2016). The discrepancy between gas-based and stellar-based determinations of the solar height is small, and thus only likely to dominate over intrinsic midplane variations on small scales, but will be relevant for detailed modeling of young and kinematically cold stars. For instance, it will induce a  $\sim 10\%$  error in  $J_z$  for an orbit with  $z_{\rm max} \sim 100$  pc.

#### 4.2.4. LSR

Finally, one must define the LSR, or mean velocity of stars near the Sun relative to the Galactic center (which is defined to have zero velocity), and the velocity of the Sun relative to the LSR. The radial  $(U_{\odot})$  and vertical  $(W_{\odot})$  components are computed by taking the mean motions of different stellar groups (e.g., Schönrich 2012). The azimuthal component  $(V_{\odot})$  is more difficult to measure, but can be modeled using the asymmetric drift relation (Binney & Tremaine 2008). The values of the components of the LSR are usually taken from Schönrich et al. (2010). Their uncertainties should also lead to systematic errors in the actions, as given in Equations (9)–(10). For example, the value of the circular velocity is taken to be  $\sim$ 220 km s<sup>-1</sup> (e.g., Bovy et al. 2012) with roughly 10% uncertainty. We expect this to translate to at least a 10% systematic error in  $J_{\phi}$ .

#### 4.3. Orbit Integration

We have mainly been concerned with actions, since they provide a convenient way to quantify different types of orbits. However, all of our conclusions also apply to studies that simply rely on orbit integrations, since the two are equivalent. For instance, computing orbital properties of open or globular clusters (e.g., Cantat-Gaudin et al. 2016, 2018; *Gaia* Collaboration et al. 2018a) should ideally take the midplane variation into account. Orbit integrations of nearby systems over short time periods (e.g., Mamajek & Bell 2014; Bailer-Jones et al. 2018) are unlikely to be impacted. It should also be unimportant for halo applications, e.g., in modeling of stellar streams (e.g., Bovy 2014) or the substructure potentially responsible for the gap in GD1 (Bonaca et al. 2019).

#### 5. Conclusions

Determining the orbital properties of stars is important for understanding the structure and evolution of the Galaxy. Actions have been argued to be excellent orbit labels. If the Galaxy can be well approximated as axisymmetric and 6D phase-space positions can be measured accurately and precisely enough, then the computed actions are invariant with orbital phase. However, we have shown that the fact that the Galactic midplane is not constant across the disk presents a significant complication to computed actions actually being invariant. Our main conclusions are:

- 1. Inaccuracy in the Galactocentric coordinate system induces orbital phase dependence in the actions calculated from the observed positions and velocities of stars (Figures 1 and 2). Since stars' instantaneous phase-space positions are measured without prior knowledge of their orbital phases, this results in systematic error in the computed actions (Figure 4).
- 2. Inaccuracy in the midplane location most severely affects computation of the vertical action  $J_z$ . A midplane offset of  $\sim 15$  pc for a typical thin disk orbit results in a 25% error in  $J_z$ , and even for a thick disk orbit a 120 pc offset will result in the same size error. The fractional error is significantly less for halo orbits.
- 3. The distribution of systematic errors in the actions induced by a coordinate system offset is highly non-Gaussian. The distribution is bimodal with *neither mode at null*. As a result, error propagation of coordinate system offsets is complex when considering actions, and is likely to significantly deform the action-space distribution function.
- 4. Dynamical modeling across large regions of the disk, over which the midplane location varies by more than the limits discussed above, is susceptible to this type of systematic error, since the assumption that our local Galactic midplane is the global Galactic midplane is not true a priori. A violation of this assumption (by, e.g., intrinsic midplane variations) leads to a systematic error in *z* which generates the large errors in actions summarized above.
- 5. We show that such midplane variation is likely by measuring the local galactic midplane along the solar circle in three different high-resolution, zoom-in simulations of Milky Way-mass galaxies from the FIRE collaboration, as well as a controlled simulation of the interaction of the Milky Way with Sagittarius. We found that the midplane varies as a function of azimuth at the solar circle by 60–185 pc in these simulations.
- 6. Assuming a vertical velocity variation of the Milky Way of ∼5−10 km s<sup>-1</sup>, consistent with recent results from *Gaia* and our results from the FIRE simulations (Figure 10), we estimated that the corresponding midplane offsets are ∼60−170 pc by dimensional analysis using the vertical frequencies of disk-like orbits. This range of values is consistent with the variations seen in the simulations. Similar offsets are seen in three-dimensional dust maps.
- 7. Inaccuracies in the parameters of the currently adopted Galactocentric coordinate system are likely important for some applications. In particular, it is imperative to test the assumption that the dynamical Galactic center is colocated with Sgr A\*. We discuss how to do this in Section 4.2.
- 8. This work underlines the importance of combining chemistry and dynamics. Since chemical tagging

- (Freeman & Bland-Hawthorn 2002) is not subject to the same systematic errors discussed in this work, it should be used to confirm dynamical associations and to offset the effect of these systematic errors on the action-space distribution function.
- 9. While in this work we have focused on systematic errors in action computation, all of our conclusions also extend to studies of stars that simply rely on orbit integration, since the computation of actions and orbit integrations are equivalent.

Our main point is that the local midplane varies between different points in the Galaxy, and that this variation can lead to significant systematic errors in the computation of actions under the assumption of a global axisymmetric potential. Current observations from Gaia should soon permit a measurement of the real azimuthal dependence of the midplane location. For some applications, such as those using actions as labels to group stars on similar orbits, using such a measurement to shift stars to a consistent midplane height as a function of azimuth before using a global axisymmetric approximation to the potential may be sufficient, although this ignores the dynamical implications of shifts in the midplane height (which result from fluctuations in the local density). However, for other applications, such as the study of action diffusion, a more extensive perturbative approach is likely needed. We plan to explore the mitigation of these effects in future work.

## 5.1. Supplementary Material

All code used in this work is available at https://github.com/gusbeane/actions\_systematic and archived at Zenodo doi:10.5281/zenodo.3364081.

We thank the anonymous referee for providing helpful comments. We would like to thank Megan Bedell, Robert A. Benjamin, Maria Bergemann, Joss Bland-Hawthorn, Tobias Buck, Elena D'Onghia, Benoit Famaey, and Adrian Price-Whelan for helpful discussions. A.B. would like to thank Todd Phillips for helpful discussions. This work uses data hosted by the Flatiron Institute's FIRE data hub. The Flatiron Institute is supported by the Simons Foundation. This project was developed in part at the 2019 Santa Barbara Gaia Sprint, hosted by the Kavli Institute for Theoretical Physics (KITP) at the University of California, Santa Barbara. This research was supported in part at KITP by the Heising-Simons Foundation and the National Science Foundation (NSF) under grant No. PHY-1748958. This work used the Extreme Science and Engineering Discovery Environment (XSEDE), which is supported by NSF grant No. OCI-1053575. A.B. was supported in part by the Roy & Diana Vagelos Program in the Molecular Life Sciences and the Roy & Diana Vagelos Challenge Award. K.V.J.'s contributions were supported in part by the NSF under grant No. AST-1614743. M.-M.M.L. was partly supported by the NSF under grant No. AST-1815461.

Software: This work made use of the following software: astropy (Astropy Collaboration et al. 2013; Price-Whelan et al. 2018), gala (Price-Whelan 2017; Price-Whelan et al. 2019), matplotlib (Hunter 2007), numpy (Van Der Walt et al. 2011), scipy (Jones et al. 2001), and tqdm (da Costa-Luis 2019).

### Appendix A Orbits

We plot the three orbits considered throughout the work (Table 1) in Figure 8.

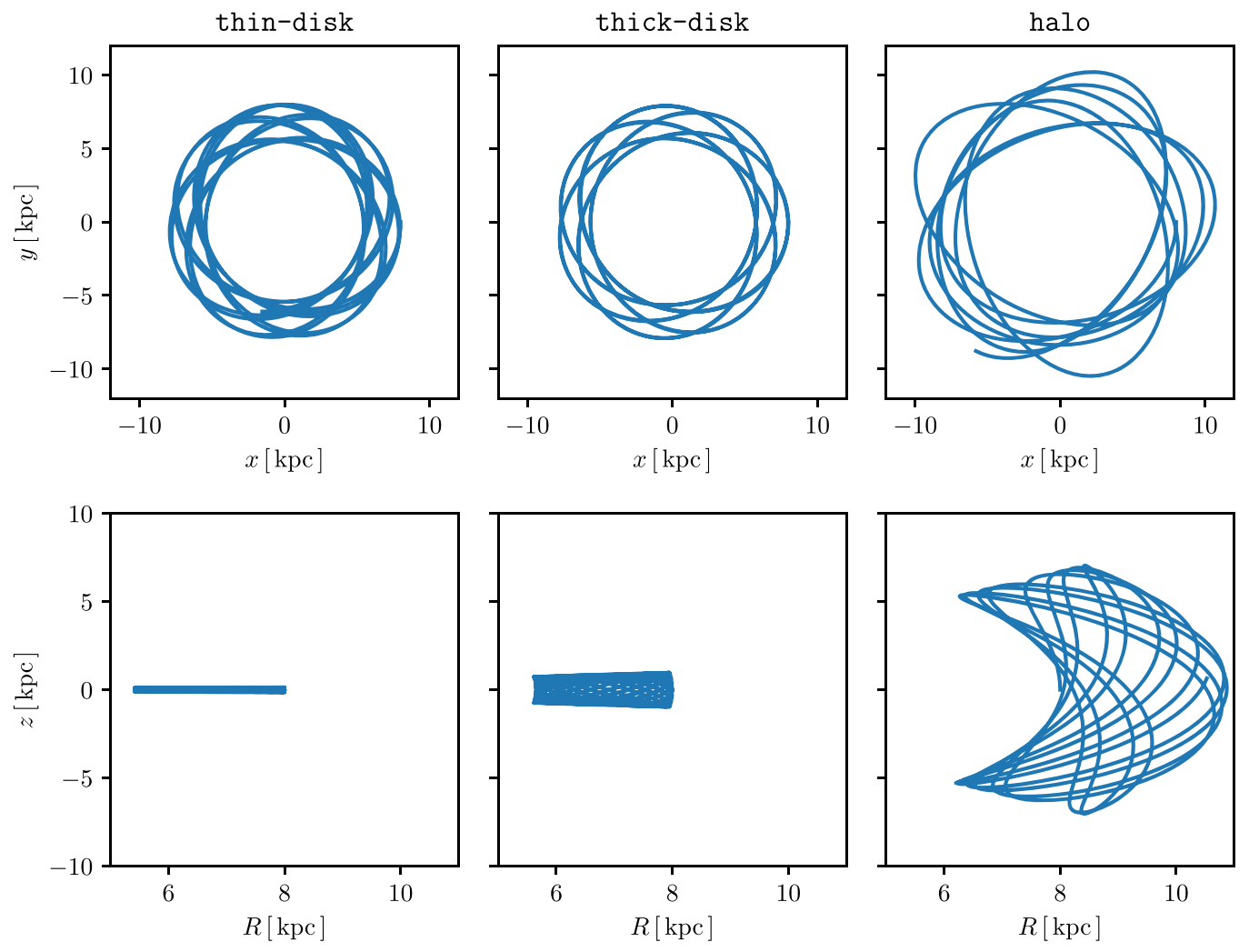


**Figure 8.** The three orbits presented in Table 1 and considered throughout the work. We plot thin-disk, thick-disk, and halo in the left, center, and right columns, respectively. The upper row shows a plot of x vs. y while the lower row shows R vs. z.

## Appendix B $\Delta R - \Delta x$ Relation

We considered the effect on actions of an inaccuracy in the distance from the Sun to the Galactic center, which introduces an offset in the x-coordinate,  $\Delta x$ , of each star when converting to a Galactocentric coordinate system. In observations of nearby stars, we have that  $\Delta x \sim \Delta R$ . However, for the experiment we performed in Section 2.4 we considered observations of a star throughout its entire orbit. Therefore, we must average  $\Delta R$  over the course of the orbit. We derive this relation now.

An offset  $\Delta x$  results in an erroneous radius  $R_{\rm err}$  related by the formula

$$(x + \Delta x)^2 + y^2 = R_{\text{err}}^2$$
 (14)

Keeping only terms to first order in  $\Delta x$ , we have that

$$R_{\text{err}}^2 = R^2 - 2R\cos\phi\Delta x$$
  

$$\Longrightarrow \Delta R \equiv |R_{\text{err}} - R| = |\cos\phi| \Delta x.$$
 (15)

Averaging over the circle, we therefore have that

$$\langle \Delta R \rangle = \frac{2}{\pi} \Delta x. \tag{16}$$

# 

In Figure 9 we plot the distribution of  $J_R$  as a function of orbital phase induced by an offset in x and z and the distribution of  $J_\phi$  for an offset in x. We plot the distributions for thickdisk (upper panels) and thin-disk (lower panels). We find that the  $J_R$  distribution induced by an offset in x more closely resembles a Gaussian distribution, while the  $J_R$  distribution induced by an offset in z and the  $J_\phi$  distribution induced by an offset in z are both similar to the  $J_z$  distribution induced by an offset in z (see Figure 3).

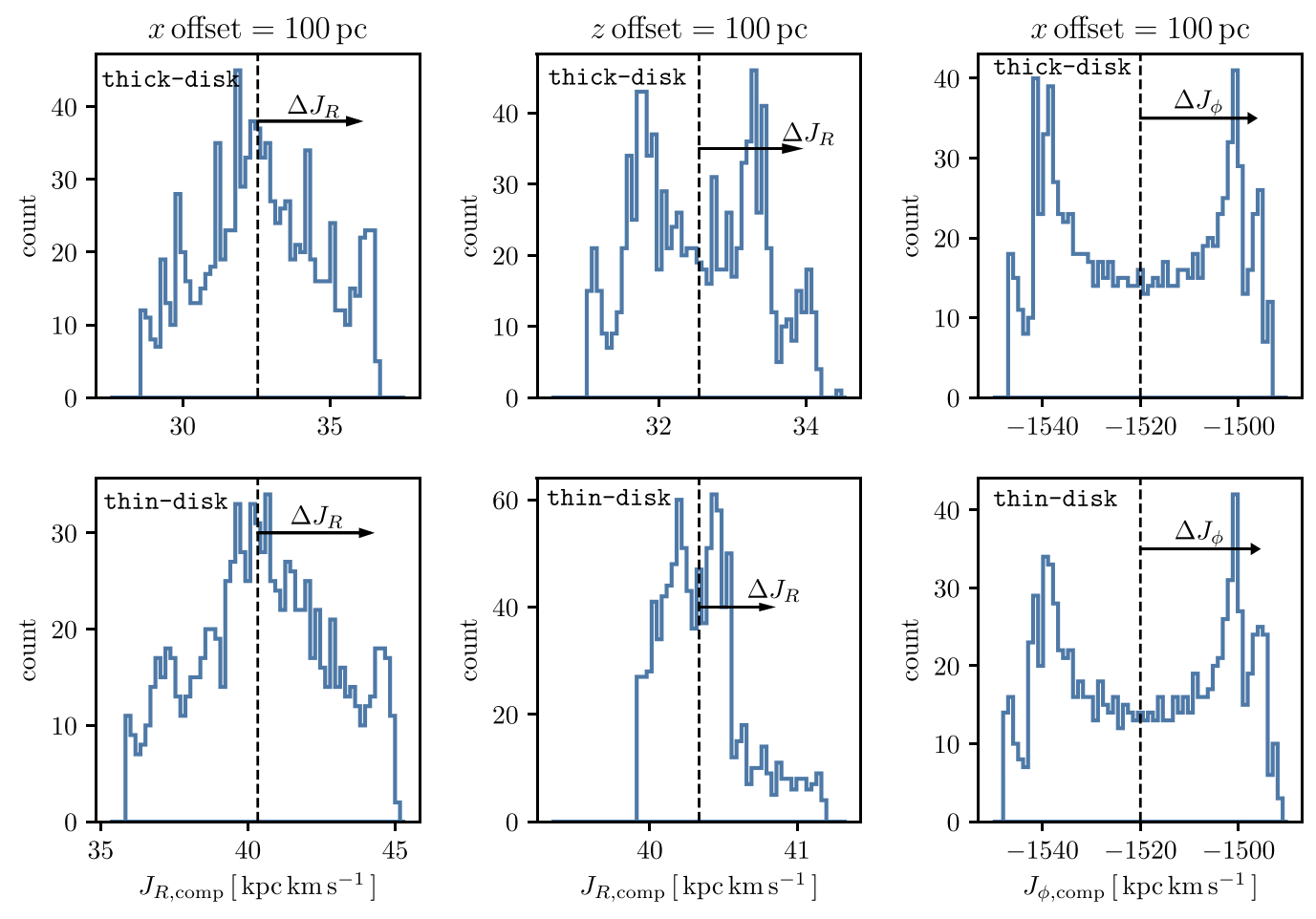


Figure 9. A histogram of the values computed for  $J_R$  and  $J_\phi$  for thick-disk (upper panels) and thin-disk (lower panels). For  $J_R$  we assume an x offset (left) and z offset (center) of 100 pc, while for  $J_\phi$  we consider only an x offset (right). In each panel the true value is given by a vertical dashed line. The induced error distribution in  $J_R$  for an x offset more closely resembles a Gaussian centered on the null value, but not for the other two offsets considered.

## Appendix D LSR Variations

We consider the variations of the LSR as a function of azimuth at the fiducial solar circle ( $R_0 = 8.2 \text{ kpc}$ ) in Figure 10.

At each azimuth,  $\phi$ , we take the median velocity in cylindrical coordinates of all stars within 200 pc of the position, following Sanderson et al. (2018). No best-fit subtraction was performed as in Figure 6.

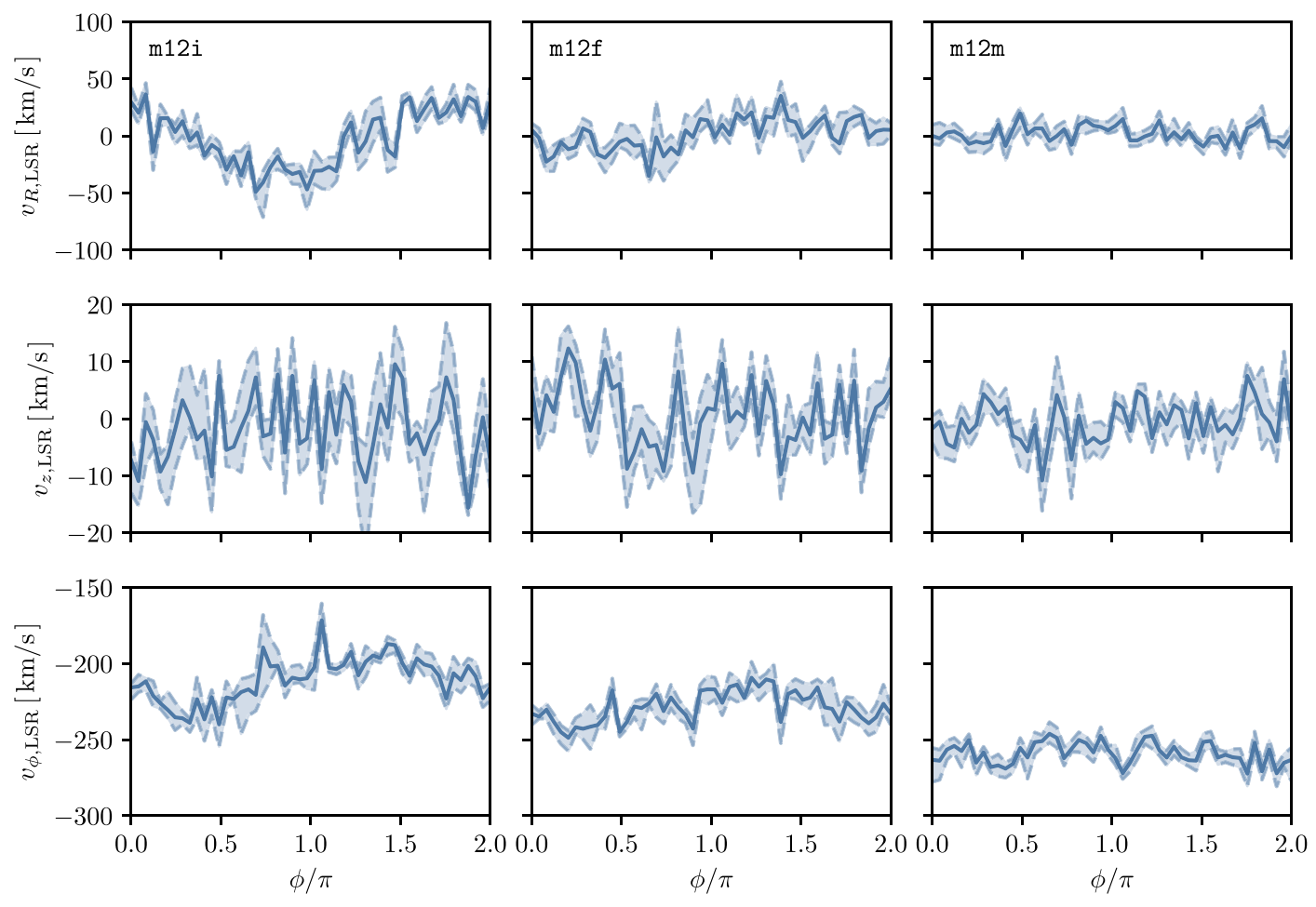


Figure 10. The LSR as a function of azimuth at the fiducial solar circle ( $R_0 = 8.2 \text{ kpc}$ ). No best-fit subtraction is performed here as we did in the case of the midplane (Section 3.3). Variations in  $v_z$  are on the order of  $\sim 5-10 \text{ km s}^{-1}$ .

Binney, J. 2012, MNRAS, 426, 1324

#### ORCID iDs

Angus Beane https://orcid.org/0000-0002-8658-1453 Robyn E. Sanderson https://orcid.org/0000-0003-3939-3297

Melissa K. Ness https://orcid.org/0000-0001-5082-6693 Douglas Grion Filho https://orcid.org/0000-0001-8275-9181

Mordecai-Mark Mac Low https://orcid.org/0000-0003-0064-4060

David W. Hogg https://orcid.org/0000-0003-2866-9403

#### References

Abuter, R., Amorim, A., Bauboeck, M., et al. 2019, arXiv:1904.05721
Anderson, L. D., Wenger, T. V., Armentrout, W. P., Balser, D. S., & Bania, T. M. 2019, ApJ, 871, 145

Anglés-Alcázar, D., Faucher-Giguère, C.-A., Kereš, D., et al. 2017, MNRAS, 470, 4698

Antoja, T., Helmi, A., Romero-Gómez, M., et al. 2018, Natur, 561, 360
Astropy Collaboration, Robitaille, T. P., Tollerud, E. J., et al. 2013, A&A, 558, A33

Bailer-Jones, C. A. L., Rybizki, J., Andrae, R., & Fouesneau, M. 2018, A&A, 616, A37

Beane, A., Ness, M. K., & Bedell, M. 2018, ApJ, 867, 31

Belokurov, V., Erkal, D., Evans, N. W., Koposov, S. E., & Deason, A. J. 2018, MNRAS, 478, 611

Bennett, M., & Bovy, J. 2019, MNRAS, 482, 1417

Bergemann, M., Sesar, B., Cohen, J. G., et al. 2018, Natur, 555, 334

```
Binney, J., & Schönrich, R. 2018, MNRAS, 481, 1501
Binney, J., & Tremaine, S. 2008, Galactic Dynamics (2nd ed.; Princeton, NJ:
  Princeton Univ. Press)
Blaauw, A., Gum, C. S., Pawsey, J. L., & Westerhout, G. 1960, MNRAS,
   121, 123
Bland-Hawthorn, J., & Gerhard, O. 2016, ARA&A, 54, 529
Bland-Hawthorn, J., Sharma, S., Tepper-Garcia, T., et al. 2019, MNRAS,
Bonaca, A., Hogg, D. W., Price-Whelan, A. M., & Conroy, C. 2019, ApJ,
  880, 38
Bovy, J. 2014, ApJ, 795, 95
Bovy, J. 2015, ApJS, 216, 29
Bovy, J., Allende Prieto, C., Beers, T. C., et al. 2012, ApJ, 759, 131
Buist, H. J. T., & Helmi, A. 2015, A&A, 584, A120
Cantat-Gaudin, T., Donati, P., Vallenari, A., et al. 2016, A&A, 588, A120
Cantat-Gaudin, T., Vallenari, A., Sordo, R., et al. 2018, A&A, 615, A49
Carlin, J. L., DeLaunay, J., Newberg, H. J., et al. 2013, ApJL, 777, L5
Chen, B., Stoughton, C., Smith, J. A., et al. 2001, ApJ, 553, 184
Chen, B. Q., Huang, Y., Yuan, H. B., et al. 2019, MNRAS, 483, 4277
Crane, J. D., Majewski, S. R., Rocha-Pinto, H. J., et al. 2003, ApJL, 594, L119
da Costa-Luis, C. O. 2019, tqdm: A Fast, Extensible Progress Meter for Python
  and CLI, version 4.32.2, Zenodo, doi:10.5281/zenodo.2800317
Das, P., Hawkins, K., & Jofre, P. 2019, arXiv:1903.09320
de Zeeuw, T. 1985, MNRAS, 216, 273
Dormand, J., & Prince, P. 1980, JCoAM, 6, 19
Feast, M. W., Menzies, J. W., Matsunaga, N., & Whitelock, P. A. 2014, Natur,
  509, 342
```

Freeman, K., & Bland-Hawthorn, J. 2002, ARA&A, 40, 487 Friske, J., & Schönrich, R. 2019, arXiv:1902.09569

Gaia Collaboration, Helmi, A., van Leeuwen, F., et al. 2018a, A&A, 616, A12

Gaia Collaboration, Katz, D., Antoja, T., et al. 2018b, A&A, 616, A11

```
Gandhi, S. S., & Ness, M. K. 2019, ApJ, 880, 134
Garrison-Kimmel, S., Hopkins, P. F., Wetzel, A., et al. 2018, MNRAS,
   481, 4133
Gillessen, S., Eisenhauer, F., Trippe, S., et al. 2009, ApJ, 692, 1075
Gómez, F. A., Minchev, I., O'Shea, B. W., et al. 2013, MNRAS, 429, 159
Goodman, A. A., Alves, J., Beaumont, C. N., et al. 2014, ApJ, 797, 53
Gravity Collaboration, Abuter, R., Amorim, A., et al. 2018, A&A, 615, L15
Green, G. M., Schlafly, E. F., Zucker, C., Speagle, J. S., & Finkbeiner, D. P.
   2019, arXiv:1905.02734
Helmi, A. 2004, ApJL, 610, L97
Helmi, A., Babusiaux, C., Koppelman, H. H., et al. 2018, Natur, 563, 85
Hernquist, L. 1990, ApJ, 356, 359
Hopkins, P. F., Kereš, D., Oñorbe, J., et al. 2014, MNRAS, 445, 581
Hopkins, P. F., Wetzel, A., Kereš, D., et al. 2018, MNRAS, 480, 800
Hunter, J. D. 2007, CSE, 9, 90
Ibata, R., Lewis, G. F., Irwin, M., Totten, E., & Quinn, T. 2001, ApJ, 551, 294
Ibata, R. A., Irwin, M. J., Lewis, G. F., Ferguson, A. M. N., & Tanvir, N. 2003,
         AS, 340, L21
Jeans, J. H. 1915, MNRAS, 76, 70
Johnston, K. V., Zhao, H., Spergel, D. N., & Hernquist, L. 1999, ApJL,
Jones, E., Oliphant, T., Peterson, P., et al. 2001, SciPy: Open source scientific
   tools for Python, version 1.3.0, http://www.scipy.org/
Jurić, M., Ivezić, Ž., Brooks, A., et al. 2008, ApJ, 673, 864
Katz, N., & White, S. D. M. 1993, ApJ, 412, 455
Kerr, F. J. 1957, AJ, 62, 93
Koppelman, H., Helmi, A., & Veljanoski, J. 2018, ApJL, 860, L11
Küpper, A. H. W., Balbinot, E., Bonaca, A., et al. 2015, ApJ, 803, 80
Lancaster, L., Koposov, S. E., Belokurov, V., Evans, N. W., & Deason, A. J.
  2019, MNRAS, 486, 378
Laporte, C. F. P., Johnston, K. V., Gómez, F. A., Garavito-Camargo, N., &
   Besla, G. 2018, MNRAS, 481, 286
Laporte, C. F. P., Johnston, K. V., & Tzanidakis, A. 2019a, MNRAS,
   483, 1427
Laporte, C. F. P., Minchev, I., Johnston, K. V., & Gómez, F. A. 2019b,
     INRAS, 485, 3134
Leike, R. H., & Enßlin, T. A. 2019, arXiv:1901.05971
Li, T. S., Sheffield, A. A., Johnston, K. V., et al. 2017, ApJ, 844, 74
Ma, X., Hopkins, P. F., Faucher-Giguère, C.-A., et al. 2016, MNRAS,
   456, 2140
Ma, X., Hopkins, P. F., Wetzel, A. R., et al. 2017, MNRAS, 467, 2430
Mackereth, J. T., Schiavon, R. P., Pfeffer, J., et al. 2019, MNRAS, 482, 3426
Mamajek, E. E., & Bell, C. P. M. 2014, MNRAS, 445, 2169
Martin, N. F., Ibata, R. A., & Irwin, M. 2007, ApJL, 668, L123
McGill, C., & Binney, J. 1990, MNRAS, 244, 634
```

McMillan, P. J. 2017, MNRAS, 465, 76

```
Meza, A., Navarro, J. F., Abadi, M. G., & Steinmetz, M. 2005, MNRAS,
  359, 93
Miyamoto, M., & Nagai, R. 1975, PASJ, 27, 533
Morganson, E., Conn, B., Rix, H.-W., et al. 2016, ApJ, 825, 140
Muratov, A. L., Kereš, D., Faucher-Giguère, C.-A., et al. 2015, MNRAS,
  454, 2691
Navarro, J. F., Abadi, M. G., Venn, K. A., Freeman, K. C., & Anguiano, B.
  2011, MNRAS, 412, 1203
Navarro, J. F., Frenk, C. S., & White, S. D. M. 1997, ApJ, 490, 493
Ness, M., Rix, H. W., Hogg, D. W., et al. 2018, ApJ, 853, 198
Newberg, H. J., Yanny, B., Rockosi, C., et al. 2002, ApJ, 569, 245
Oñorbe, J., Garrison-Kimmel, S., Maller, A. H., et al. 2014, MNRAS,
  437, 1894
Price-Whelan, A., Sipocz, B., Lenz, D., et al. 2019, adrn/gala: v1.0, Zenodo,
  doi:10.5281/zenodo.2638307
Price-Whelan, A. M. 2017, JOSS, 2, 388
Price-Whelan, A. M., & Bonaca, A. 2018, ApJL, 863, L20
Price-Whelan, A. M., Johnston, K. V., Sheffield, A. A., Laporte, C. F. P., &
  Sesar, B. 2015, MNRAS, 452, 676
Price-Whelan, A. M., Sipőcz, B. M., Günther, H. M., et al. 2018, AJ, 156, 123
Reid, M. J., & Brunthaler, A. 2004, ApJ, 616, 872
Sanders, J. L., & Binney, J. 2014, MNRAS, 441, 3284
Sanders, J. L., & Binney, J. 2016, MNRAS, 457, 2107
Sanders, J. L., & Das, P. 2018, MNRAS, 481, 4093
Sanderson, R. E., Helmi, A., & Hogg, D. W. 2015, ApJ, 801, 98
Sanderson, R. E., Wetzel, A., Loebman, S., et al. 2018, arXiv:1806.10564
Schönrich, R. 2012, MNRAS, 427, 274
Schönrich, R., Binney, J., & Dehnen, W. 2010, MNRAS, 403, 1829
Sellwood, J. A. 2014, RvMP, 86, 1
Sellwood, J. A., Trick, W. H., Carlberg, R. G., Coronado, J., & Rix, H.-W.
  2019, MNRAS, 484, 3154
Sharma, S., Johnston, K. V., Majewski, S. R., et al. 2010, ApJ, 722, 750
Sheffield, A. A., Johnston, K. V., Majewski, S. R., et al. 2014, ApJ, 793, 62
Sheffield, A. A., Price-Whelan, A. M., Tzanidakis, A., et al. 2018, ApJ, 854, 47
Silverwood, H., & Easther, R. 2018, arXiv:1812.07581
Slater, C. T., Bell, E. F., Schlafly, E. F., et al. 2014, ApJ, 791, 9
Ting, Y.-S., & Rix, H.-W. 2018, ApJ, 878, 21
Trick, W. H., Bovy, J., D'Onghia, E., & Rix, H.-W. 2017, ApJ, 839, 61
Trick, W. H., Coronado, J., & Rix, H.-W. 2019, MNRAS, 484, 3291
Van Der Walt, S., Colbert, S. C., & Varoquaux, G. 2011, arXiv:1102.1523
Villumsen, J. V., & Binney, J. 1985, ApJ, 295, 388
Wetzel, A. R., Hopkins, P. F., Kim, J.-H., et al. 2016, ApJL, 827, L23
Widrow, L. M., Gardner, S., Yanny, B., Dodelson, S., & Chen, H.-Y. 2012,
Williams, M. E. K., Steinmetz, M., Binney, J., et al. 2013, MNRAS, 436, 101
Xu, Y., Newberg, H. J., Carlin, J. L., et al. 2015, ApJ, 801, 105
```